Oxytocin neurons signal state-dependent transitions from rest to thermogenesis and behavioral arousal in social and non-social settings

Morgane Vandendoren[1#], Jason G. Landen[1#], Joseph F. Rogers[1#], Samantha Killmer[1], Baizar Alimiri[1], Celeste Pohlman[1], Glenn J. Tattersall[2], Nicole L. Bedford[1], Adam C. Nelson[1*]

1) Department of Zoology and Physiology, University of Wyoming, Laramie, WY, USA.
2) Department of Biological Sciences, Brock University, St Catharines, Ontario, Canada

[#] These authors contributed equally

* Corresponding author: Adam C Nelson, anelso74@uwyo.edu

Abstract
Core body temperature (Tb) is defended within narrow limits through thermoregulatory behaviors like huddling, nesting, and physical activity as well as autonomic responses like brown fat thermogenesis and peripheral vasodilation. While Tb displays regulated fluctuations across different behavioral states and rest/arousal cycles, the neural control of these transitions is poorly understood. Here, we investigate the relationship between oxytocin neurons of the paraventricular hypothalamus (PVN^{OT}) and behavioral and autonomic thermoeffector pathways across physiological states in mice. First, we show that PVN^{OT} neurons are activated during social thermoregulation. We then demonstrate that—in both social and nonsocial contexts—in vivo PVN^{OT} calcium dynamics align with transitions from rest to thermogenesis and behavioral arousal. Using a computer vision model to track thermoeffector pathways, we demonstrate that precisely timed stimulation of PVN^{OT} during low-Tb resting states increases thermogenesis and behavioral arousal. We therefore suggest a model in which PVN^{OT} neurons facilitate state-dependent transitions in thermo-behavioral states.

Introduction

Maintaining a relatively constant core body temperature (Tb) is a vital homeostatic need. While excessive deviations (e.g. >2°C) from the typical mammalian Tb of approximately 37°C can be harmful (Nixdorf-Miller et al., 2006), Tb normally fluctuates within a narrow range (typically 0.5 - 1°C) across sleep-wake cycles and behavioral states (Blessing and Ootsuka, 2016; Refinetti, 2020, 1999). These fluctuations often exhibit bimodal or multimodal distributions, indicating distinct thermal states. Additionally, Tb variations are increasingly understood not as passive outcomes of animal physiology, but as regulated, brain-initiated transitions between defended Tb "balance-points" (Romanovsky, 2018) (Blessing and Ootsuka, 2016; Morrison and Nakamura, 2019; Škop et al., 2024). For example, the transition from the rest to the active balance-point involves modulation of both autonomic and behavioral thermoeffector pathways (i.e., regulated heat loss and production) to meet the energetic demands of movement and arousal (Blessing and Ootsuka, 2016; Harding et al., 2020; Škop et al., 2024). However, the neural mechanisms that govern these physiological transitions remain incompletely understood (Harding et al., 2020, 2019).

Thermoregulation is orchestrated by the integration of autonomic and behavioral effectors. Autonomic outputs, such as brown adipose tissue (BAT) thermogenesis and vasomotor tone, are well-characterized at the circuit level. This pathway integrates sensory signals from peripheral thermosensors in the preoptic area of the hypothalamus (POA), then relays this information to the dorsomedial hypothalamus (DMH), and then to sympathetic efferent neurons of the rostral medullary raphe (rMR) (Morrison, 2011; Morrison and Nakamura, 2019). By contrast, the neuronal substrates of behavioral thermoregulation—such as huddling, nesting, or physical activity (Gordon, 2012; Landen et al., 2024; Škop et al., 2024, 2021)—and how they integrate with autonomic outputs are less well defined. Although recent studies have made progress in identifying brain regions underlying some of the associated neural pathways, (Almeida et al., 2015; Jung et al., 1998; Sotelo et al., 2022; Tan and Knight, 2018), much remains unknown about how animals behaviorally thermoregulate.

Behavioral thermoregulation strategies are naturally organized into alternating sequences across bouts of arousal and quiescence and are modulated by environmental conditions (including social context) and internal state (Endo et al., 2018; Gordon et al., 2014; Harding et al., 2020, 2019; Landen et al., 2024; Sotelo et al., 2024, 2022). Huddling is a cooperative behavior that provides thermal and energetic benefits through shared body heat and reduction of heat loss (Alberts, 1979; Fransson et al., 2005; Gilbert et al., 2010; Haig, 2008). When mice experience mild cold stress, huddling facilitates both entry into, and exit from, an energy-saving, low-Tb quiescent state (Landen et al., 2024). This pattern suggests active neural regulation of behavior and sympathetic arousal in tandem; however, the brain circuits that support this coordination remain unidentified.

Oxytocin (OT)-producing neurons in the paraventricular nucleus of the hypothalamus (i.e., PVN^{OT}) are a compelling candidate for such coordination (Rogers et al., 2024). PVN^{OT} neurons have been implicated in autonomic arousal (Chen et al., 2021), energy expenditure (Noble et al., 2014), and thermoregulation—including activation of BAT thermogenesis (Fukushima et al., 2022; Kasahara et al., 2013; Sutton et al., 2014). The oxytocin system is also classically associated with social behaviors (Froemke and Young, 2021) including physical touch (Tang et al., 2020)—a key element of huddling. Indeed, OT-mutant rat pups display deficits in both warm-seeking and huddling behavior (Harshaw et al., 2018), and OT neurons display bursts of pulsatile activity during bouts of lactation and direct physical contact with pups (Yaguchi et al., 2024). Yet, whether PVN^{OT} neural activity is functionally associated with the organization of thermoregulatory states is not known.

Here, we set out to identify the relationship between PVN^{OT} activity and daily patterns of behavioral thermoregulation in mice. We initially observed that PVN^{OT} activity is linked to huddling states. Then, we discovered that PVN^{OT} calcium dynamics during huddling are predictive of transitions to body warming and arousal. Intriguingly, in a parallel fashion, PVN^{OT} activity also tracks transitions from rest to arousal in solo animals. Last, using automated thermal feature tracking and optogenetics, we demonstrate that PVN^{OT} stimulation initiates state-dependent transitions that coordinate physiological warming with behavioral arousal. These findings reveal a previously unrecognized role for PVN^{OT} neurons in regulating dynamic, context-dependent thermo-behavioral strategies.

Results

PVN^{OT} neural activity is associated with huddling substates.

Mice use huddling to facilitate thermoregulatory state transitions. We sought to identify huddling-associated brain regions in groups of adult females, which show stronger huddling-associated Tb changes than male groups (Landen et al., 2024). Using a home-cage surveillance system that eliminates direct human-animal interaction (Landen et al., 2024) in conjunction with FOS immunohistochemistry (IHC), we examined patterns

of neural FOS activity in 18 brain regions. We focused on regions associated with thermoregulation, social behavior, and identified to be FOS-activated during huddling substates in preliminary studies (Fig. 1A-B). We examined animals engaged in active huddling (close physical contact while displaying some physical activity), quiescent huddling (close physical contact with no physical activity) and—as a control for physical touch in the absence of social contact—solo-housed animals engaged in self-grooming. For IHC, we scored cellular FOS activity after the animals had been engaged in state-specific behavior (i.e., active huddle, quiescent huddle, solo-groom) for at least 15 minutes.

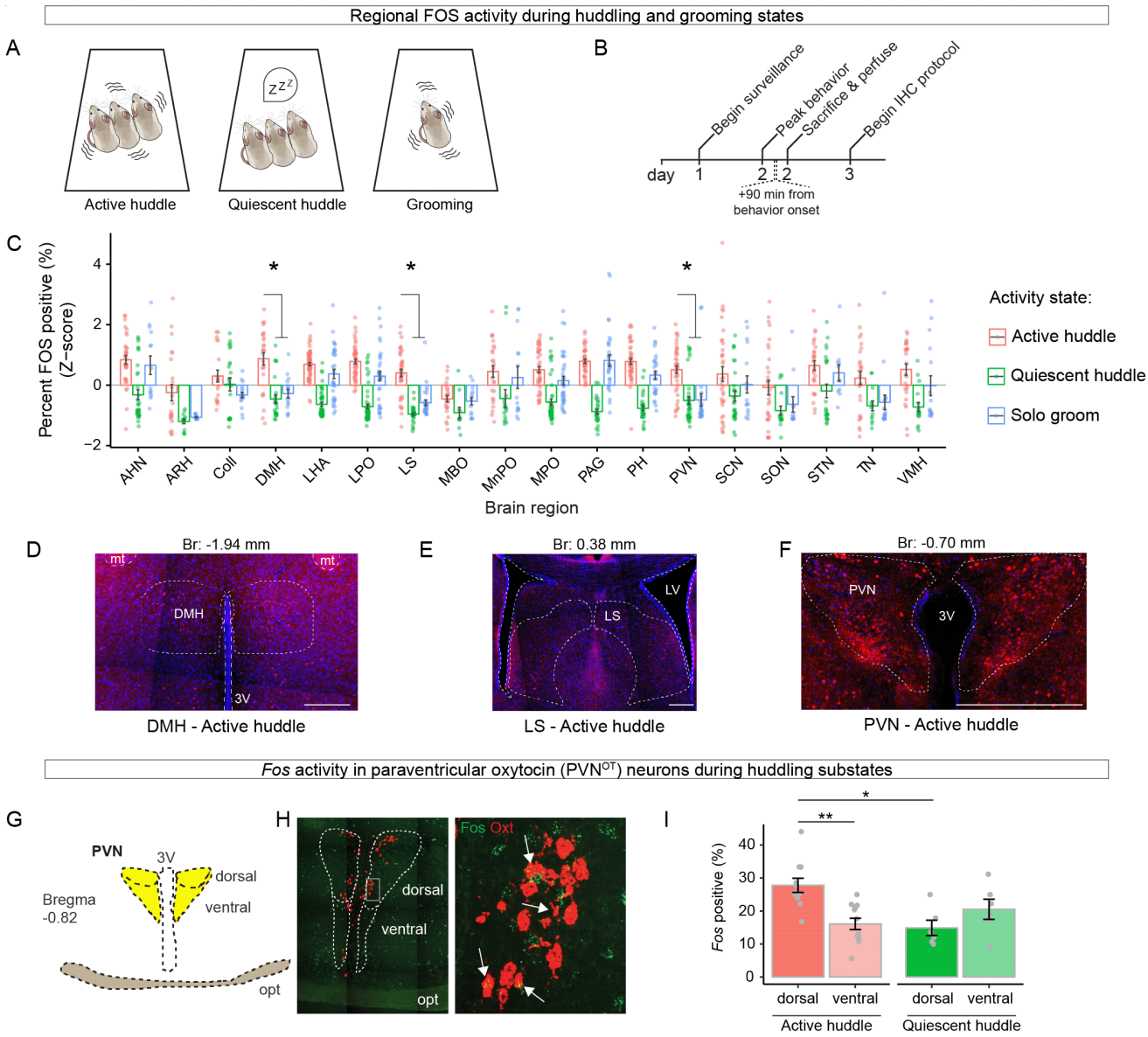

Figure 1. The PVN and PVN^{OT} neurons are FOS activated during huddling substates.
(A - B) Experimental design to identify state-specific activity in 18 brain regions. Behavioral states **(A)**. Experimental timeline **(B)**.
(C) Quantification of percent FOS - DAPI colocalized cells across brain regions for each behavior. Regional FOS percentages are z-scored on a per experiment basis. N = 15 mice/1530 ROIs. Each datapoint is an ROI. Asterisks denote regions in which active huddle FOS activity is greater than both quiescent huddle and solo groom. P-values adjusted for multiple comparisons using the Holm method.
(D - F) Representative histology images showing active huddling associated FOS expression in the DMH **(D)**, LS **(E)**, and PVN **(F)**. 3V: third ventricle; mt: mammillothalamic tract; LV: lateral ventricle. Scale bar equals 500 µm.
(G) Schematic of the PVN. Opt: optic tract.
(H) Representative histology images showing mRNA expression of *Fos* and *Oxt* in the PVN.
(I) Quantification of percent *Fos*:DAPI colocalized cells in dorsal and ventral subregions of the PVN during active huddling and quiescent huddling (N = 8 mice). Each datapoint is an ROI.
C: linear model with Tukey's post-hoc tests. **I:** linear mixed effect model. Data are mean ±SEM. P < 0.05 *, P < 0.01 **, P < 0.001 ***. Full statistical analysis in Table S1.

We initially focused on active huddling-associated FOS expression because this state requires that an animal actively maintain close physical contact with another individual. We identified three regions that were activated 90 minutes after the onset of active-huddling: the dorsal medial hypothalamus (DMH), the rostral lateral septum (LS), and the paraventricular nucleus of the hypothalamus (PVN) (Fig. 1C-F and S1A-C; all statistical results are reported in Table S1). The DMH and the PVN are areas associated with energy regulation and thermoregulation, with inputs to the rMR (Morrison et al., 2014; Morrison and Nakamura, 2019; Seoyoung Son et al., 2022). The LS is associated with a variety of functions, from motivation to fear responses (Besnard and Leroy, 2022; Rizzi-Wise and Wang, 2021) and is strongly associated with the control of social behavior (Menon et al., 2022). These results suggest active huddling recruits brain regions with known roles in thermoeffector and social interaction pathways.

The PVN is one of two primary locations of OT-producing neurons (Seoyoung Son et al., 2022). Given the established associations of PVN^{OT} neurons with thermoregulation and social behavior, we asked whether they were activated during active and quiescent huddling. To increase the temporal resolution of our assay from the timescale of protein translation to that of mRNA transcription, we used single-molecule fluorescence *in situ* hybridization (smFISH) to identify PVN^{OT} neurons that became *Fos*-positive 30 minutes after the onset of a behavioral state. We quantified neurons in the dorsal and ventral PVN, which have unique cyto-architectures and projection patterns (Biag et al., 2012) (Fig. 1G-I). PVN^{OT} neurons were *Fos*-positive during both active huddling and quiescent huddling. During active huddling, the dorsal population was more *Fos*-positive than the ventral population, and this dorsal population displayed greater *Fos* activity during active compared to quiescent huddling (Fig. 1I).

These results suggest the PVN is a huddling-associated brain region and that PVN^{OT} neurons are activated during huddling substates. Given the coarse timescale of *Fos* dynamics (≥30 minutes) compared to the faster timescale of rest-arousal cycles in mice (minutes; (Li et al., 2022; McShane et al., 2010)), we next employed in vivo calcium recordings to capture finescale population-level dynamics of PVN^{OT} neurons.

PVN^{OT} Ca^{2+} peaks track rest and arousal behavior states in social and non-social conditions.
Behaviorally, mice modulate body temperature through physical activity, nesting, and huddling (Gordon, 2012; Landen et al., 2024; Škop et al., 2024, 2021). In a longitudinal study accounting for individual variance in physiology and behavior, we next asked how calcium activity in PVN^{OT} neurons was associated with real-time behavior during social thermoregulation in different thermal conditions (Fig. 2A-C). As a control for social context, we also examined solo-housed animals. Experiments were conducted at three floor temperatures: cold (15°C), cool (23°C; room temperature), and a temperature near the "lower critical temperature" (29°C; the transition point between energy-requiring and energy-neutral thermoregulatory mechanisms (Gordon, 2012; Maloney et al., 2014; Škop et al., 2020)). We tracked six behaviors in the solo condition and 10 behaviors in the paired condition (Fig. 2B).

We used an AAV encoding the calcium indicator GCaMP (pGP-AAV9-syn-FLEX-jGCaMP8s-WPRE) (Zhang et al., 2023) and fiber photometry using an optical fiber implanted above the PVN (Fig. 2A-D). GCaMP AAVs have been validated to transfect OT neurons in OT-Cre mice (Resendez et al., 2020; Yukinaga et al., 2022; Zhan et al., 2024) and, in this study, showed co-labelling with OT-immunoreactive neurons (Fig. S2A-B). Neural-photometric recordings were conducted during the light/rest phase, when the distinction between different thermoregulatory states is more discernable (Landen et al., 2024). We observed large calcium transients (hereafter "peaks") that appeared to be similar to those previously reported in lactating female mice (Yaguchi et al., 2024; Yukinaga et al., 2022) (Fig. 2D). Further analyses focused on peaks that were at least six standard deviations above baseline.

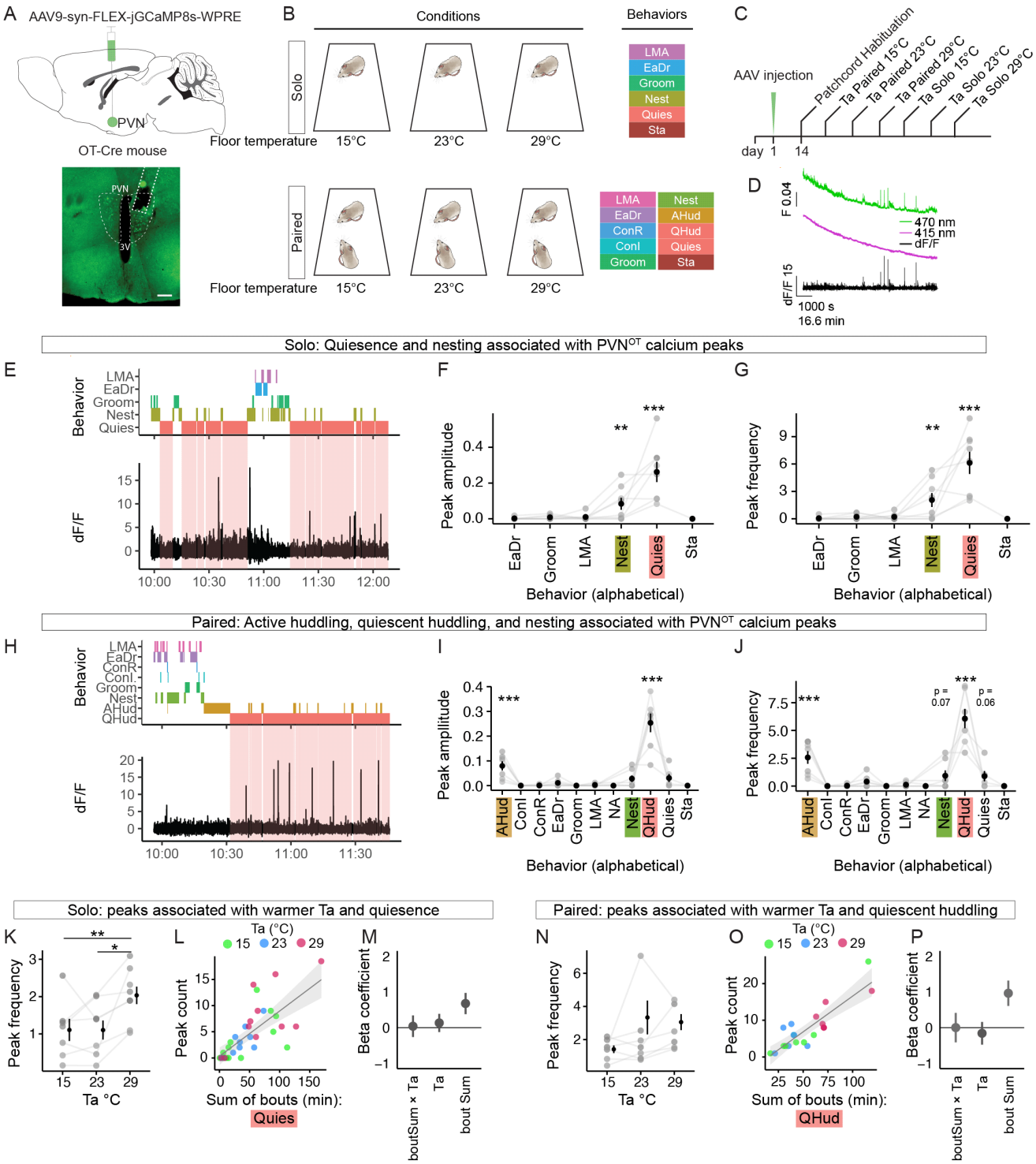

Figure 2. PVN^OT peaks track rest and arousal behavior states in social and non-social conditions.
(A - C) Fiber photometric recordings of PVN^OT cells in different social contexts and floor temperature conditions. Scheme of GCaMP AAV injections (top) and histology showing GCaMP-positive neurons in the PVN optic fiber placement (bottom) Scale bar 200 µm. **(A)**. Floor temperature and social context conditions, and behaviors analyzed **(B)**. Scheme of the timeline. Order of the social and floor temperature conditions was pseudo-randomized **(C)**.
(D) Example traces of calcium-dependent (470 nm) and calcium-independent (415 nm) channels, and the post-processed dF/F trace (bottom), from a two-hour recording.
(E - G) Behaviors associated with PVN^OT peaks in solo condition. Example ethogram aligned to photometric recording. Soft red shaded areas align with the quiescent state **(E)**. PVN^OT peak amplitude **(F)** and frequency **(G)** according to behavioral state across solo trials.
(H - J) Behaviors associated with PVN^OT peaks in paired condition. Example ethogram aligned to photometric recording. Soft red shaded areas align with quiescent huddling **(H)**. PVN^OT peak amplitude **(I)** and frequency **(J)** according to behavioral state across paired trials.

Figure 2 cont'd. (K - M) Effect of floor temperature and quiescence on PVN^{OT} peaks in solo animals. Peak frequency according to floor temperature (Ta) **(K)**. Peak count according to total duration of quiescent bouts **(L)**. Beta coefficients from a model of the effect of floor temperature, total duration of bouts (boutSum), and the Ta*boutSum interaction on peak count **(M)**.
(N - P) Effect of floor temperature and quiescence huddling on PVN^{OT} peaks in paired animals. PVN^{OT} peak frequency according to floor temperature **(N)**. Peak count according to total duration of quiescent bouts **(O)**. Beta coefficients from a model of the effect of floor temperature, total duration of bouts (boutSum), and the Ta*boutSum interaction on peak count **(P)**.
F,G,I,J,K,L,M,N,O,P: linear mixed model. N = 8 mice/50 recordings. **M** and **P** show means plus confidence interval; all else shows mean ±SEM. $P < 0.05$ *, $P < 0.01$ **, $P < 0.001$ ***. Full statistical analysis in Table S1.

We first examined the effect of social context (i.e., paired- vs. solo-housed) on calcium peak amplitude and frequency across the three floor temperatures. While there was no effect of social context on peak amplitude (Fig. S2C), there was an increase in peak frequency in paired animals (Fig. S2C-D). To our surprise, in both social and nonsocial contexts, PVN^{OT} peaks were strongly linked to specific behaviors. In the solo context, peak amplitude and frequency were associated with nesting and quiescence (i.e., motionless rest) (Fig. 2E-G). In the paired context, peaks were associated with active and quiescent huddling (Video S1) and, to a lesser extent, nesting (Fig. 2H-J). We next examined the behavioral associations of PVN^{OT} peaks within each floor temperature. The behavior-state associations with calcium peaks were largely preserved across all three floor temperatures (Fig. S2G-J). Linear mixed model analysis of calcium peak amplitude and frequency revealed main effects of quiescence and nesting in the solo context (Fig. S3G,I), and main effects of active huddling, quiescent huddling, and nesting in the paired context (Fig. S3H,J). Thus, PVN^{OT} peaks are associated with distinct resting and waking behavioral states in social and non-social contexts.

Next, we analyzed the relationship between floor temperature and peak frequency across the two social contexts (Fig. 2K-P). Peaks were more frequent 29°C for both solo (Fig. 2K) and paired (Fig. 2N) animals. In mice, sleep is more common at warmer ambient temperatures (Harding et al., 2020). To disambiguate whether PVN^{OT} peaks display warm sensitivity vs. arousal-state dependency, we performed a multiple regression analysis relating the number of peaks to floor temperature and the duration of rest bouts (i.e., quiescence quiescent huddling) (Fig. 2F-G and I-J). In both the solo and paired conditions, calcium peak counts were strongly related to rest bout duration (Fig. 2L,O). Moreover, quiescence and quiescent huddling bouts appeared longer at 29°C (Fig. 2L,O, red dots). We therefore examined the contribution of bout length and floor temperature to peak counts. In the solo and paired contexts, increased peak counts at 29°C could be explained by longer rest bout lengths (Fig. 2M and 2P).

Together, these results suggest PVN^{OT} peaks track distinct resting and active behaviors in social and non-social settings, and are slightly enhanced in the social context. In addition, PVN^{OT} peaks are largely unaffected by the ambient temperature conditions tested; we therefore pooled data from the three floor temperatures in subsequent analyses.

PVN^{OT} neurons predict transitions towards thermogenesis and behavioral arousal in social and non-social contexts.

PVN^{OT} peaks track two rest states (quiescence and quiescent huddling), and two active states (i.e., nesting and active huddling) (Fig. 2). Notably, each of these states are in part thermoregulatory and are naturally organized into alternating sequences of bouts across rest/active cycles (Endo et al., 2018; Gordon et al., 2014; Harding et al., 2020, 2019; Landen et al., 2024; Sotelo et al., 2024, 2022). To address how PVN^{OT} dynamics align with these sequences, we quantified peaks relative to the onset and offset of behavior bouts, as well as to changes in physical activity and core body temperature (Fig. 3A).

We first examined physical activity (as measured by frame-to-frame pixel changes) before and after PVN^{OT} calcium peaks in the home-cage. In both solo and paired conditions, physical activity increased following PVN^{OT} peaks. This increase began at the approximate time of the peak and persisted through the subsequent 400 seconds (6.6 min) (Fig. 3B-E). We next examined the density (i.e., frequency of peaks per time bin) of calcium peaks with respect to the onset and offset of the two resting states: quiescence and quiescent huddling. For both behaviors, there was a higher density of peaks in the minutes prior to bout offset compared to onset (Fig. S3A-C). Moreover, there was a positive relationship between bout length and the number of peaks per bout, indicating that longer rest bouts are more likely to have peaks (Fig. S3B,D). To better understand the relationship between PVN^{OT} dynamics and bouts of quiescence and quiescence huddling, we examined (1) the per-second probability of observing a peak relative to bout onset/offset using logistic regression, and (2) changes in calcium baseline (Fig. 3F-M).

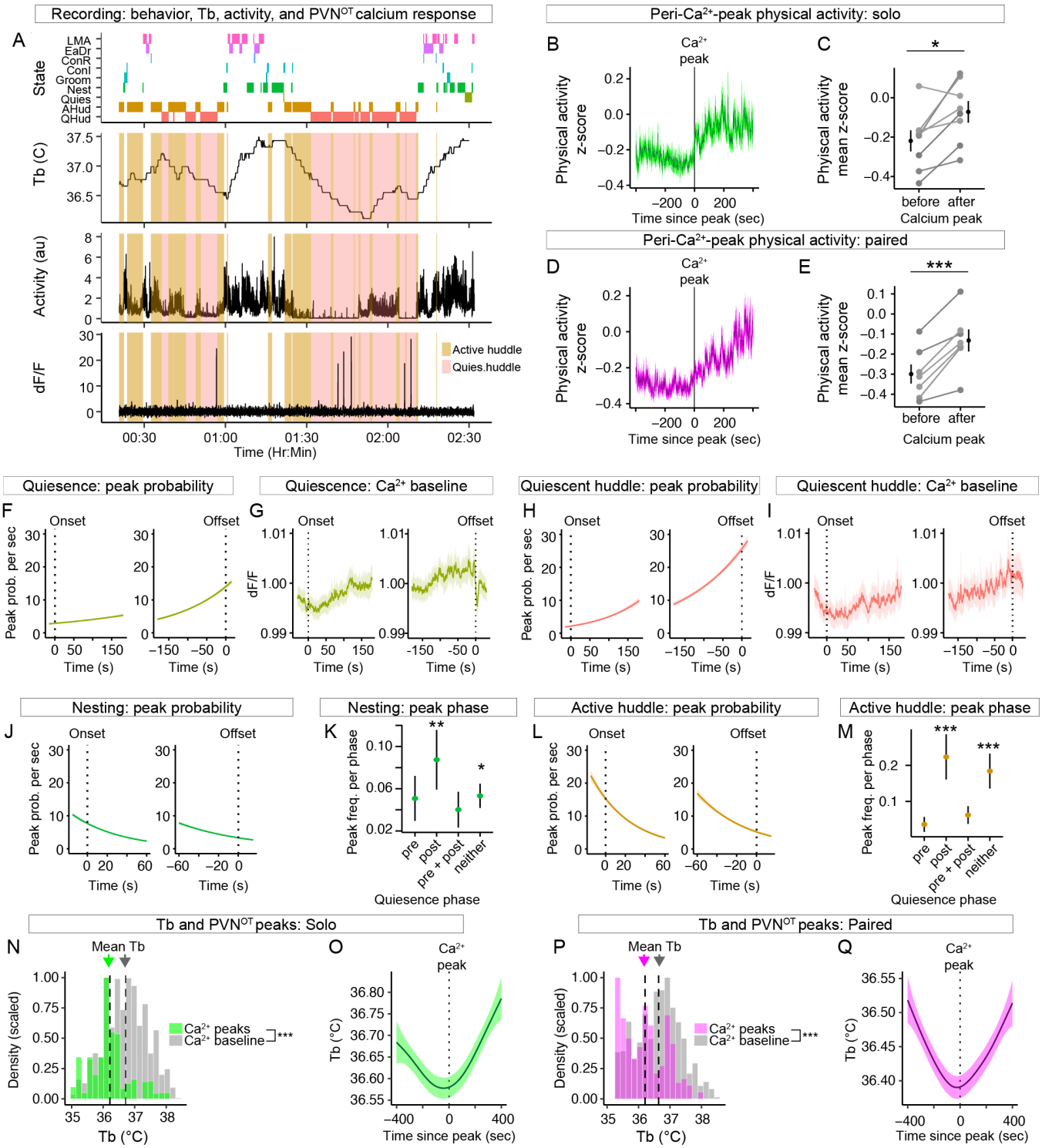

Figure 3. PVN^{OT} peaks predict transitions to behavioral arousal and thermogenesis.

(A) Alignment of behavioral state, body temperature, physical activity, and dF/F from an experiment in the paired context. Bouts of active- and quiescent-huddle are color coded.

(B - E) Physical activity around the time of PVN^{OT} peaks. Peri-event time histogram of activity before and after PVN^{OT} peaks in solo mice **(B)**. Per-individual means before and after PVN^{OT} peaks in solo mice **(C)**. Peri-event time histogram of activity before and after peaks in paired mice **(D)**. Per-individual means before and after peaks in paired mice **(E)**.

(F - I) PVN^{OT} Ca^{++} dynamics during onset and offset of rest-behavior bouts. Quiescence onset/offset: peak probability **(F)** and Ca^{++} baseline average **(G)**. Quiescent huddle onset/offset: peak probability **(H)** and Ca^{++} baseline average **(I)**.

(J - M) PVN^{OT} Ca^{++} dynamics during onset and offset of active-behavior bouts. Nesting onset/offset: peak probability **(J)**. Nesting-associated peak frequency according to quiescence phase. "Neither" refers to bouts not adjoining bouts of quiescence **(K)**. Active huddle onset/offset: peak probability **(L)**. Active-huddle-associated peak frequency according to quiescence phase. "Neither" refers to bouts not adjoining bouts of quiescence **(M)**.

Figure 3 cont'd. (N - Q) PVN^{OT} Ca^{++} dynamics and core body temperature. Histogram of body temperature during minutes containing a calcium peak (green) vs. baseline (grey) data in solo animals **(N)**. Peri-event time histogram of body temperature before and after PVN^{OT} peaks in solo animals **(O)**. Histogram of body temperature during minutes containing a calcium peak (green) vs. baseline (grey) data in paired animals **(P)**. Peri-event time histogram of body temperature before and after PVN^{OT} peaks in paired animals **(Q)**.
C,E,K,M,N,P: linear mixed model. **F,H,J,L**: logistic regression. N = 8 mice/50 recordings, except for **N-Q**, N = 5 mice/24 recordings. **O** and **Q** show predicted values of a general additive model ±SEM; all data shows mean ±SEM. $P < 0.05$ *, $P < 0.01$ **, $P < 0.001$ ***. Full statistical analysis in Table S1.

For bouts of quiescence, peak probability was approximately 2.7% near the time of onset and 14.0% near the time of offset (Fig. 3F). For bouts of quiescent huddling, peak probability was approximately 2.1% near the onset and around 25.6% near the time of offset (Fig. 3H). In accordance with the peak density and probability data, baseline calcium in PVN^{OT} neurons was higher in the minutes leading to quiescence offset compared to onset in all animals (Fig. 3G,I and S3I-J). Thus, PVN^{OT} neural activity strongly predicts quiescence/quiescent huddling offset compared to onset by at least five-fold, and signals an increase in physical activity—a correlate of behavioral arousal (De Lecea et al., 2012) and a means of increasing metabolic rate and Tb (Gordon, 1993).

We next examined PVN^{OT} peak density and probability during the onset and offset of the two active states: nesting and active huddling (Fig. 3J-M, and S3E-H). In contrast to the two resting states, peak density in both states was higher near bout onset compared to offset (Fig. S3E,G). Moreover, there was only a weak relationship between peak count and bout length for both states, indicating that longer bouts are not more likely to have peaks (Fig. S3F,H). Logistic regression analysis of nesting bouts showed that PVN^{OT} peak probability was approximately 7.7% near the time of onset and 3.3% near the time of offset (Fig. 3J). For active huddling bouts, peak probability was approximately 15.3% near the time of onset and 5.2% near the time of offset (Fig. 3L). Thus, for nesting and active huddling, PVN^{OT} peaks are two- to three-fold more likely to predict bout onset than offset. Notably, within the paired condition, there was a higher peak probability for active huddling compared to nesting (Poisson regression, nesting vs. active huddling peaks counts, $P < 0.001$), suggesting that social interaction enhances the probability of PVN^{OT} activity.

Nesting and active huddling often occur immediately before or after (or in between) bouts of quiescence (i.e., the peri-quiescent phase) (Gordon et al., 2014; Landen et al., 2024; Sotelo et al., 2024, 2022). We next examined the quiescence phase for PVN^{OT} peaks associated with nesting and active huddling. PVN^{OT} peaks were more likely to occur during the post-quiescence phase for both nesting (Fig. 3K) and active huddling (Fig. 3M). Notably, although nesting and active huddling are commonly expressed during the pre-quiescent phase, these two behaviors are rare during the post-quiescent phase (Fig. S3K-L). Thus, even though nesting and active huddling are relatively rare during the post-quiescent phase, those are precisely the active states during which PVN^{OT} activity increases. These results suggest PVN^{OT} neurons distinguish nesting/active huddling in the post-quiescent phase from these same behaviors in the pre-quiescent phase.

Together these results suggest that PVN^{OT} activity dynamics predict within approximately 100 seconds the offset of two rest states (quiescence and quiescent huddling) and within around 20 seconds the onset of two post-quiescence active states (nesting and active huddling) in solo and paired mice, respectively.

PVN^{OT} peaks occur during low Tb (~36.2°C) and prior to body warming.
In rodents, transitions from rest to arousal are thought to result, in part, from an ultradian (i.e., occurring on cycles < 24 hr), brain-driven switch of the defended body temperature from a rest balance-point (i.e., lower bound) to an awake balance-point (i.e., upper bound) (Blessing and Ootsuka, 2016; Škop et al., 2024). Because PVN^{OT} calcium peaks aligned with transitions from resting to active states, we next examined individual core Tb dynamics before, during, and after PVN^{OT} peaks (Fig. 3N-Q). In both solo and paired conditions, PVN^{OT} peaks occurred when Tb was around 0.5°C lower than baseline (baseline-Tb: 36.7°C; peri-peak-Tb: 36.2°C) (Fig. 3N,P). Moreover, PVN^{OT} peaks aligned with the low point of a U-shaped body temperature profile: on average, Tb decreased before, and increased after, the time of the calcium peak in both solo and paired conditions (Fig. 3O,Q). Together, these results suggest that PVN^{OT} peaks occur during a low Tb and predict a forthcoming increase in Tb.

Validation of PVN^{OT} neural calcium peaks.
PVN^{OT} neurons display pulsatile activity bursts during lactation and direct contact with pups, with heightened intensity and broadening waveforms during late-stage lactation (PPD 8 to 14) compared to early-stage lactation (PPD 2-7) (Yaguchi et al., 2024; Yukinaga et al., 2022; Yukinaga and Miyamichi, 2025). However, the extent to which this type of activity in PVN^{OT} neurons is exclusive to lactation and nursing events remains a matter of

debate (Perkinson et al., 2021; Resendez et al., 2020; Yaguchi et al., 2024). To address whether peaks occurring during transitions from quiescence to active states resemble those during lactation, we recorded from virgin females as described above and then allowed them to reproduce and nurse their young (Fig. 4A-C). As documented in other studies (Yaguchi et al., 2024; Yukinaga et al., 2022), PVN^{OT} neurons displayed peaks that increased in frequency and amplitude from early-stage to late-stage lactation—an observation that provides physiological verification of the oxytocinergic identity of the recorded neurons in our system (Fig. 4D-E and Video S2). PVN^{OT} peaks in virgin females appeared similar in amplitude in early-stage compared to late-stage lactation and appeared narrower overall (Fig. F-H). Systematic comparisons of peak kinetics revealed that virgin female calcium peaks displayed narrower full-width half maximum (FWHM) values than either early-stage or late-stage lactation (Fig. 4H-I). Next, while virgin and early-stage lactation peak amplitudes were equivalent, both were less than that of late-stage lactation (Fig. 4J). Finally, while virgin interpeak intervals (IPIs) were equivalent to early-stage lactation, they were longer than those of late-stage lactation (Fig. 4K). Together, these results suggest that PVN^{OT} peaks observed in the virgin females of this study during naturalistic home-cage behaviors share similar calcium kinetics to those during early-stage, but not late-stage lactation. As such, this data uncovers a behavioral and physiological context in which PVN^{OT} neurons display calcium burst-like peaks.

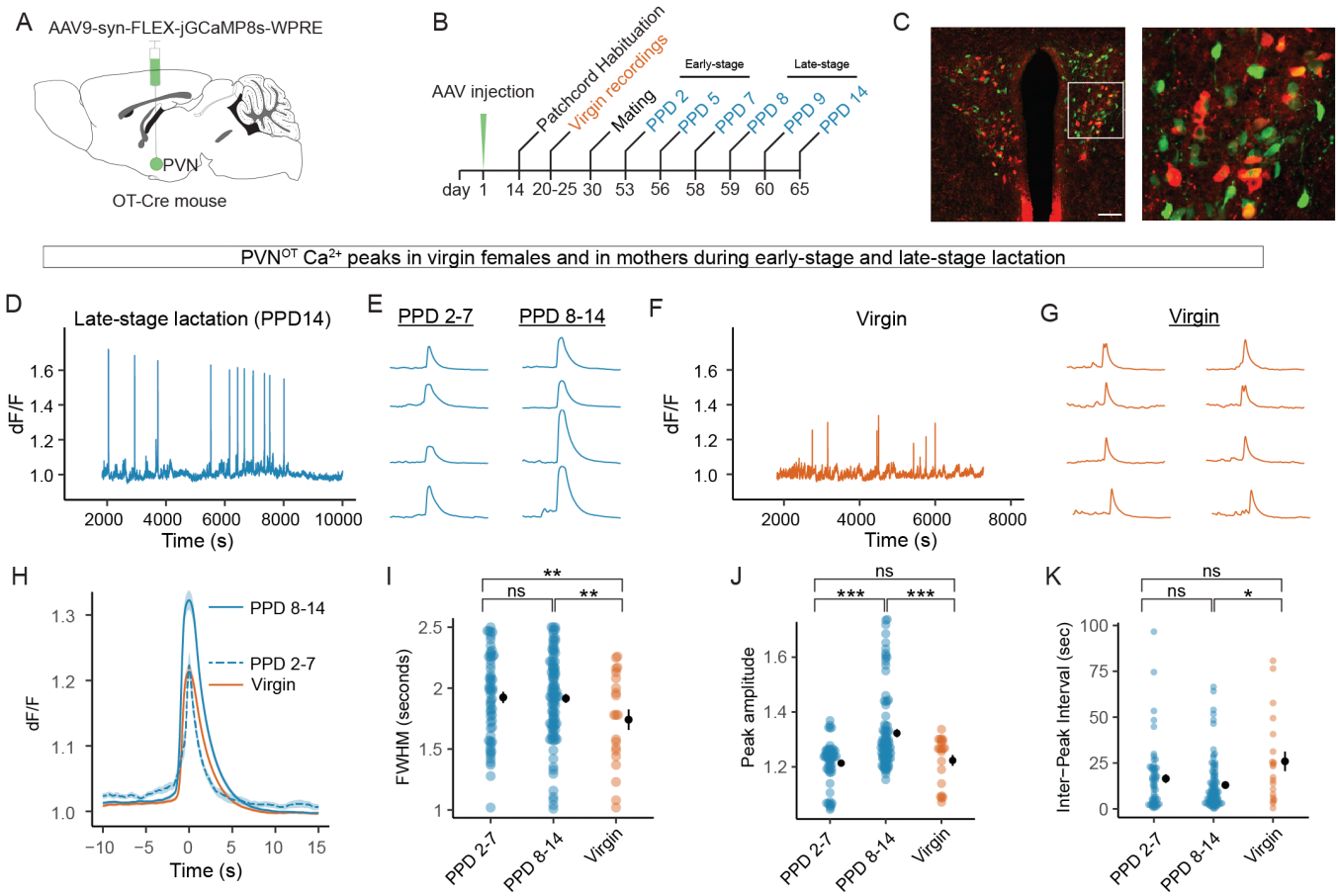

Figure 4. PVN^{OT} peaks observed in virgin females share characteristics with peaks seen in lactating mothers.
(A - C) Longitudinal fiber photometry recordings of PVN^{OT} cells in virgin-to-lactating mice. Scheme of GCaMP8s AAV injections **(A)** and recording timeline **(B)**. Typical histology section showing PVN stained with anti-OT (red) and GCaMP8s expression (green). Scale bar 100 µm. **(C).**
(D - G) PVN^{OT} Ca^{++} peaks in virgin females and in mothers during early-stage (PPD 2-7) and late-stage (PPD 8-14) lactation. Example of a dF/F trace from a two-hour recording on PPD 14 **(D)**. Representative peaks from PPD 2-7 and PPD 8-14 **(E).** Example of a post-processed dF/F trace from a two-hour recording of a virgin female **(F)**. Representative peaks **(G)**.
(H - K) PVN^{OT} Ca^{++} peak kinetics in virgins and lactating mothers. Average peaks dF/F over time of peaks according to condition **(H)**. Full-width of half maximum (FWHM) **(I)**, peak amplitude **(J)**, and interpeak interval **(K)** according to female condition. N = 2 females, N = 24 recordings, N = 174 peaks. Full statistical analysis in Table S1.

PVN^{OT} peaks signal increases in BAT thermogenesis and vasomotor tone.
Our data suggest PVN^{OT} peaks signal transitions towards thermogenesis and arousal as measured by core Tb and physical activity. However, core Tb represents the integration of several different thermoeffector pathways like BAT thermogenesis and vasomotor responses. We therefore sought to automate a computational strategy that uses video thermography recordings of awake, behaving animals to approximate BAT thermogenesis and vasomotor processes at sub-second resolution—a timescale relevant to sympathetic activity.

We developed a computer vision system called Skeleton-Guided Bodypart Segmentation (SGBS) that uses deep learning to record the surface temperature of three thermal features of an animal: the surfaces over (1) interscapular brown fat (BAT), (2) the rump, and (3) the entire dorsal surface (Fig. 5A). Our pipeline integrates DeepLabCut-based animal tracking (Mathis et al., 2018) and Mask R-CNN technologies (He et al., 2017) in a Python framework (TorchVision maintainers and contributors, 2016) to process high-resolution thermography (FLIR) videos. An attention layer integrates 10 anatomical skeleton keypoints (e.g., head, nose, shoulders and tail) with a model trained on manual annotations of the three thermal features. Leveraging these keypoints, SGBS can precisely localize and delineate thermal features for mask prediction (Fig. 5B). SGBS detects above-average temperatures in the BAT region and below-average temperatures rump region without the need for shaving the back—a manipulation alters heat loss and can alter behavioral and autonomic thermoregulation (Meyer et al., 2017)(Fig. 5C). Moreover, SGBS demonstrates 100-fold lower loss compared to an unmodified Mask R-CNN using identical training data (Fig. 5D). We used SGBS to segment BAT, rump, and dorsal surface features on a frame-by-frame basis, extracting the mean temperature for each feature (Fig. 5A and Video S3). SGBS data were synchronized with timestamps and integrated with other data streams, including calcium traces and behavior tracking. For these analyses, solo-housed females were used to eliminate the confounding effects of heat exchange with social partners.

To test the performance of SGBS, we examined the temporal dynamics of pairwise combinations of the three thermal features with respect to core Tb and identified the lag time that gives the best correlation (i.e., cross-correlation analysis) (Fig. 5E). Core and dorsal surface temperatures were very similar with no lag. Next, changes in core Tb lagged changes in BAT by approximately 90 seconds, a result consistent with a previous report (Ootsuka et al., 2009). Finally, rump temperature lagged core Tb by 20 seconds. Thus, SGBS captures the dynamics of thermoregulatory features at the resolution of seconds. These results support the notions that (1) core and dorsal surface temperatures are highly correlated because they both integrate multiple thermoeffector pathways, (2) BAT thermogenesis can drive temperature increases in the mouse body on the order of minutes, and (3) vasomotor processes in the rump regulate Tb on a relatively faster timescale (i.e., seconds) (Blessing et al., 2016).

We next used SGBS to align thermal feature data with PVN^{OT} calcium peaks from fiber photometry recordings (Fig. 5F-M). Consistent with our previous core Tb measurements (Fig. 3N-Q), BAT and dorsal surface temperatures trended downward before the calcium peak but increased afterward, a shift confirmed by a significant difference in slope before *vs*. after the peak (Fig. 5H,J). Moreover, BAT and dorsal surface temperatures were significantly greater after the peak compared to before (Fig. 5I,K). By contrast, although rump temperature showed no difference in slope before *vs*. after peak, the mean temperature was lower after the peak compared to before (Fig. 5L-M). Together, these results suggest that PVN^{OT} activity is associated with a thermogenic state characterized by the onset of BAT thermogenesis and, to a lesser degree, increased rump vasoconstriction, following PVN^{OT} activation.

Optogenetic activation of PVN^{OT} neurons initiates thermogenic responses.
To elucidate the functional link between PVN^{OT} activity during quiescence and thermoeffector outputs, channelrhodopsin (AAVDJ-EF1a-DIO-hChR2(H134R)-EYFP-WPRE-pA) was expressed in the PVN of Oxytocin-Cre mice (ChR2+) to allow for optogenetic stimulation of PVN^{OT} neurons (Fig. 6A). To control for potential warm-sensitive physiological responses due to heat from light stimulation, a “light-only” cohort of Oxytocin-Cre mice received optic fiber implants over the PVN. These experiments were conducted at room temperature (23°C) in solo-housed females to focus on the precise physiology of PVN^{OT} neurons and to eliminate confounding effects of social-partners. Blue light stimulation (10 Hz; 20 ms pulse width (20% duty cycle); 10 mW power; 10 or 20 sec pulse train) occurred after solo animals had been quiescent for at least two minutes (a condition similar to when PVN^{OT} calcium peaks occur).

We first examined the effect of blue light stimulation of PVN^{OT} neurons on core Tb. Approximately 400 sec (6.6 min) after a 20 sec, but not a 10 sec, pulse train, Tb increased in ChR2+ but not light-only controls (Fig. S4A).

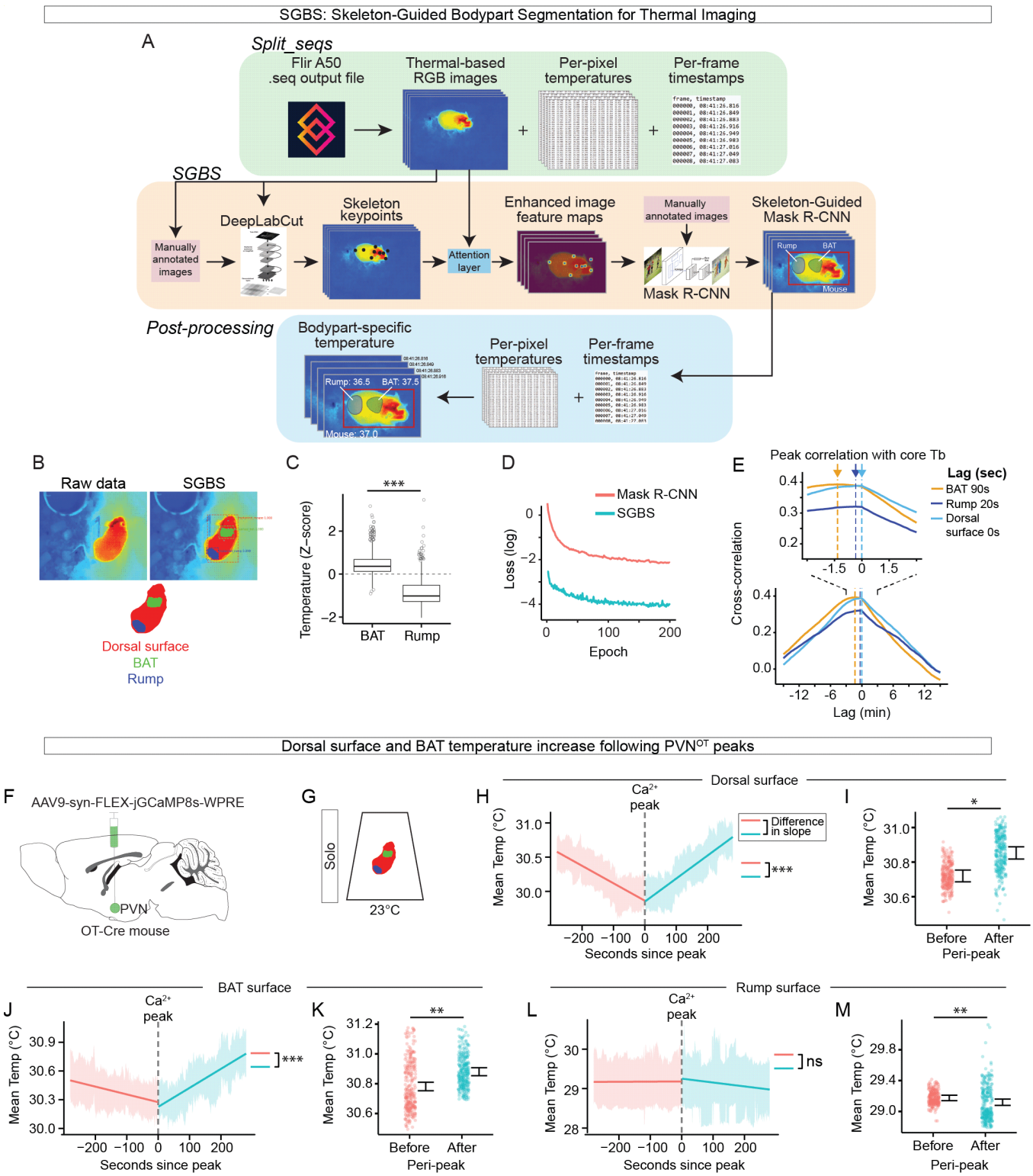

Figure 5. A computer vision model for tracking thermal features during Ca^{++} imaging.
(A) SGBS model architecture. Three main modules are involved in thermographic identification of surface temperature features: processing raw FLIR .seq files (*Split_seqs*); segmentation of anatomical regions (*SGBS*); overlaying temperatures onto segmented regions for each frame (*Post-processing*).
(B) Example image showing segmentation of three anatomical thermal features.
(C) Boxplot shows per-minute mean temperatures (BAT, rump) scaled on a per-mouse basis.
(D) Loss values between *SGBS* and traditional Mask R-CNN.
(E) Cross-correlation analysis of core body temperature (Tb) and thermal features (BAT, rump, dorsal surface). Data are from light-only control animals recorded for two hours (N = 4). A negative value in the time-shift axis means the thermal features are shifted behind relative to Tb.
(F-G) Alignment of SGBS thermal feature data with calcium imaging. Viral strategy **(E)** and experimental condition **(F)**.
(H-M) Peristimulus time histograms (PSTH) of SGBS thermal feature data in relation to the time of PVN^{OT} calcium peaks (time 0). Dorsal surface PSTH slopes **(H)** and means **(I)**. BAT surface PSTH slopes **(J)** and means **(K)**. Rump surface PSTH slopes

Figure 5 cont'd. H, J, L slope-lines are fitted values from a linear mixed model. **I, K, M** are per-frame means; statistics from a linear mixed model. G-L show means ±SEM. P < 0.05 *, P < 0.01 **, P < 0.001 ***. Full statistical analysis in Table S1.

Further examination of Tb data revealed that some blue light stimulations occurred during a relatively high Tb—in contrast to the low Tb context in which PVN^{OT} calcium peaks naturally occur (Fig. 3N-Q). To address a possible mismatch in internal physiology during optogenetic stimulations vs. endogenous calcium peaks, we stratified the data according to whether Tb was above or below average (per-mouse) at the time of stimulation (i.e., Tb-T0). The low Tb-T0 distribution was similar to the Tb distribution observed during PVN^{OT} calcium peaks in solo animals (Fig. 6B blue line, cf. Fig. 3N). We then examined the effect of 20 sec optogenetic stimulation in the stratified data and found ChR2+ stimulation caused increased Tb in the low Tb-T0 context but not the high Tb-T0 context; this increased Tb was observable 420 sec after stimulation and persisted for several minutes (Fig. 6C). Thus, precisely timed, context-dependent stimulation of PVN^{OT} neurons is sufficient to increase core Tb.

Next, we examined the effect of PVN^{OT} stimulation on physical activity and behavior (Fig. 6D, S4B-C). While no significant differences were detected between ChR2+ and controls, ChR2+ mice showed a trend toward increased physical activity over time in the low Tb-T0 context (Fig. 6D). A separate slope-based analysis of post-stimulation activity revealed that ChR2+ animals exhibited a steeper increase in physical activity compared to light-only controls in the low (but not high) Tb-T0 context. (Fig. S4C). Analysis of manually-annotated behaviors suggested that PVN^{OT} stimulation did not activate a specific motor pattern output but instead resulted in combined increases in the time spent in nesting (linear mixed model estimate coefficient of ChR2+ stimulation: +38.0 sec), locomotion (+54.0 sec), and grooming (+14.5 sec), but not in eating/drinking (-0.4 sec) (Fig. S4B).

We next examined the effect of light stimulation on thermal features using SGBS. Compared to light-only controls, 20 sec pulse trains triggered increased BAT and rump surface temperatures in the low (but not high) Tb-T0 context approximately 360 sec post stimulus (Fig. 6E-F). Moreover, in the low Tb-T0 context, blue light stimulation in ChR2+ animals increased the slopes of the surface temperatures of BAT and rump surface temperatures compared to light-only control animals (Fig. S4D-F). In contrast, in the high Tb-T0 context, blue light stimulation did not affect the BAT or rump surface temperatures and caused a slight decrease in the dorsal surface temperature (Fig. S4D-F).

These data suggest that 20 seconds of PVN^{OT} stimulation during the low Tb-T0 resting states is sufficient to trigger a sustained increase in Tb, and to a lesser extent, an increase in physical activity. Thus, PVN^{OT} neurons signal state dependent transitions in thermogenesis and behavioral arousal.

PVN^{OT} cellular projections to the rMR.

We next asked what pathways could PVN^{OT} neurons promote transitions towards thermogenesis and physical activity. rMR efferent neurons regulate non-shivering thermogenesis, cutaneous vasoconstriction, and heart rate (Morrison and Nakamura, 2019), and the surrounding gigantocellular reticular nucleus (GiA) regulates locomotion and movement (Brownstone and Chopek, 2018; Engmann et al., 2020). In rats, PVN^{OT} to rMR projections (PVN^{OT}→rMR) stimulate thermogenesis and cardiovascular responses in an oxytocin receptor (OXTR)-dependent fashion (Fukushima et al., 2022). To investigate possible PVN^{OT}→rMR cell types in mice, we used tracing tools to disambiguate magno- vs. parvocellular PVN^{OT} projections (Althammer and Grinevich, 2018) (Fig. S5A-C). The majority of PVN^{OT}→rMR projections were non-magnocellular cells located in the caudal and lateral PVN, suggesting they are parvocellular (i.e., $PVN^{OT(parvo)}$) (Fig. S5C), consistent with previous studies (Althammer and Grinevich, 2018; Fukushima et al., 2022; Li et al., 2024). In addition, we observed OXTR-positive neurons in the rMR and GiA (i.e., rMR^{OXTR}) using smFISH (Fig. S5D). Thus, $PVN^{OT(Parvo)}$→rMR^{OXTR} neurons are a candidate pathway underlying transitions towards thermogenesis and behavioral arousal in mice.

Conclusions

This study uncovers a distinct functional pattern of state-dependent PVN^{OT} activity during natural patterns of thermoregulatory and arousal behaviors. We initially set out to examine the role of PVN^{OT} neurons in social thermoregulation. Leveraging long-duration in vivo recordings, we identified large PVN^{OT} calcium peaks that emerged approximately one hour into the home-cage recording. To our surprise, these peaks were observed in both social and non-social contexts. PVN^{OT} peaks were temporally aligned with transitions from resting states

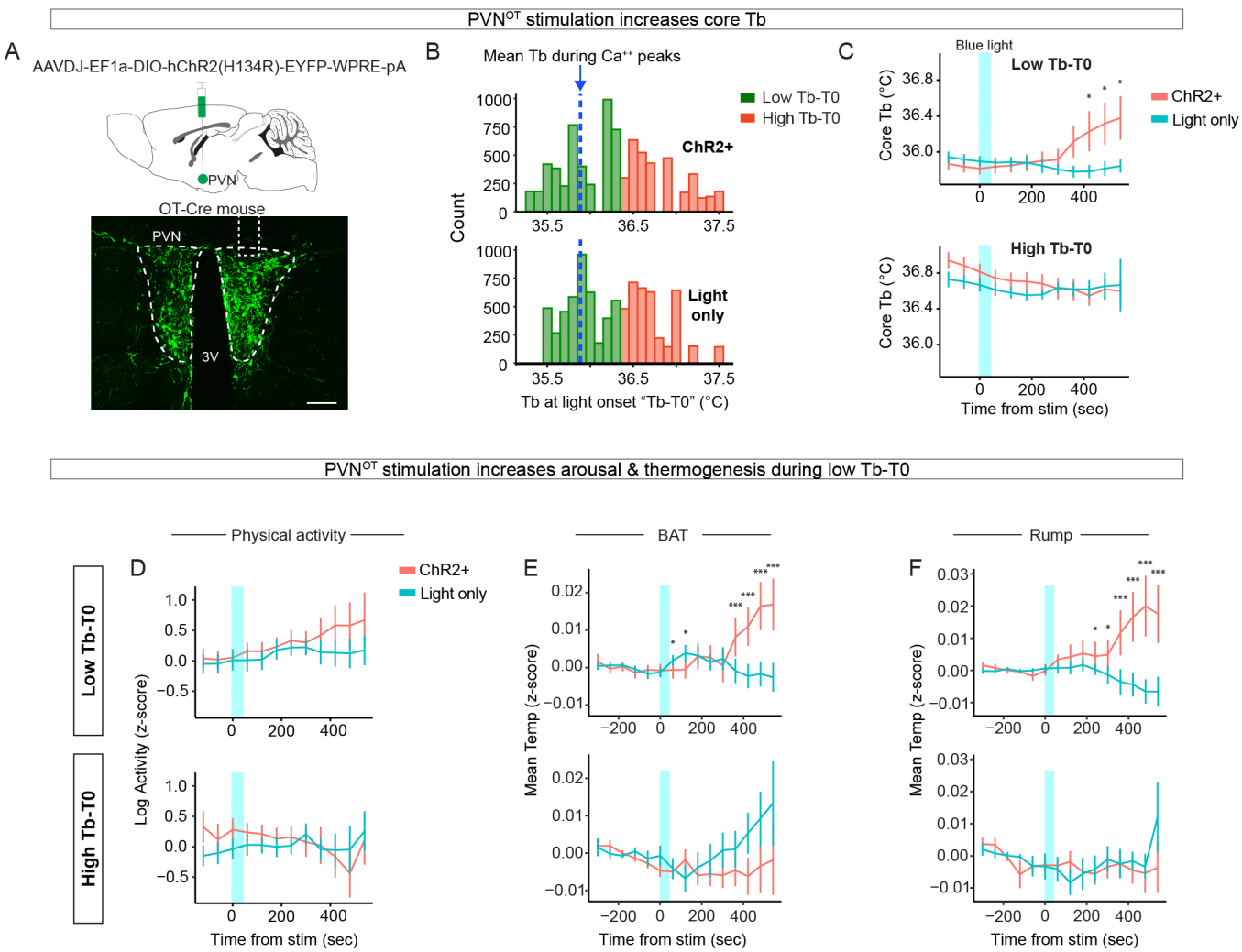

Figure 6. Optogenetic stimulation of PVN^{OT} neurons at a low Tb increases behavioral arousal and thermogenesis.
(A) Viral strategy for ChR2 transfection.
(B) Histograms showing core body temperature (Tb) during light stimulations in ChR2+ and light-only controls. Tb-T0 is the Tb at the onset of light stimulation pulse-trains. Low Tb-T0 (green) refers to stimuli during low Tb, and High Tb-T0 (red) refers to stimuli during high Tb. Blue dotted line denotes the mean Tb at which PVNOT Ca^{++} occur (from Fig. 3N).
(C) Blue light stimulation (time 0; shaded blue rectangle) increases core Tb during low Tb-T0 in ChR2+ animals compared to light-only animals (top). No effect during high Tb-T0 (bottom).
(D - F) PVN^{OT} stimulation increases arousal and thermogenesis in ChR2+ but not light-only controls. Shown are effects during low Tb-T0 (top row) and high Tb-T0 (bottom row). Optogenetic stimulation (time 0; shaded blue rectangle) triggers increases in physical activity **(D)**, BAT surface temperature **(E)**, and rump surface temperature **(F)** in ChR2+ compared to light-only control animals.
C-F: linear mixed model on data binned per-minute. Data show means ±SEM. N = 6 mice (3 ChR2+ animals and 3 light-only controls); N = 12 experiments; N = 73 light stimuli. P < 0.05 *, P < 0.01 **, P < 0.001 ***. Full statistical analysis in Table S1.

(quiescence and quiescent huddling) to active states (nesting, active huddling, and physical activity) and increased thermogenesis. Notably, the PVN^{OT} activity patterns and kinetics we observed in virgin female mice resemble the well-characterized bursts observed during the early stages of lactation (Yaguchi et al., 2024, 2023; Yukinaga et al., 2022), suggesting a broader physiological role for oxytocin neurons in coordinating transitions between thermoregulatory and behavioral states.

PVN^{OT} dynamics were temporally aligned to the offset of a low-Tb resting state. In the minutes prior to the end of a rest bout, baseline calcium increased and large peaks occurred in a probabilistic fashion: there was an approximately 20% chance of peaks occurring within around 100 seconds prior to quiescence offset, as opposed to ~2.5% during the first 100 seconds of rest onset. In addition, PVN^{OT} calcium peaks occurred more consistently when core Tb was relatively low—approximately 36.2°C, which is about 0.5°C below the average rest-phase Tb for C57B/6 animals in our colony (Landen et al., 2024). In mice, Tb displays an ultradian rhythm characterized by limit-cycle-like oscillations between biologically constrained upper and lower bounds (Blessing and Ootsuka, 2016; Škop et al., 2024). A Tb threshold of 36.2°C may represent an approximate lower-bound

of the resting state and a point at which a transition to the active-state upper-bound is initiated (Škop et al., 2024). PVN^{OT} neurons might therefore signal the transition toward thermogenesis and arousal during ultradian cycles of rest-to-arousal during the light phase. Supporting this interpretation, PVN^{OT} calcium activity and optogenetic stimulation during a low Tb—but not a high Tb—rest state signaled increases in Tb and locomotor activity within a few minutes. This state-dependency indicates that these neurons integrate information to modulate sympathetic activation (Fig. 7).

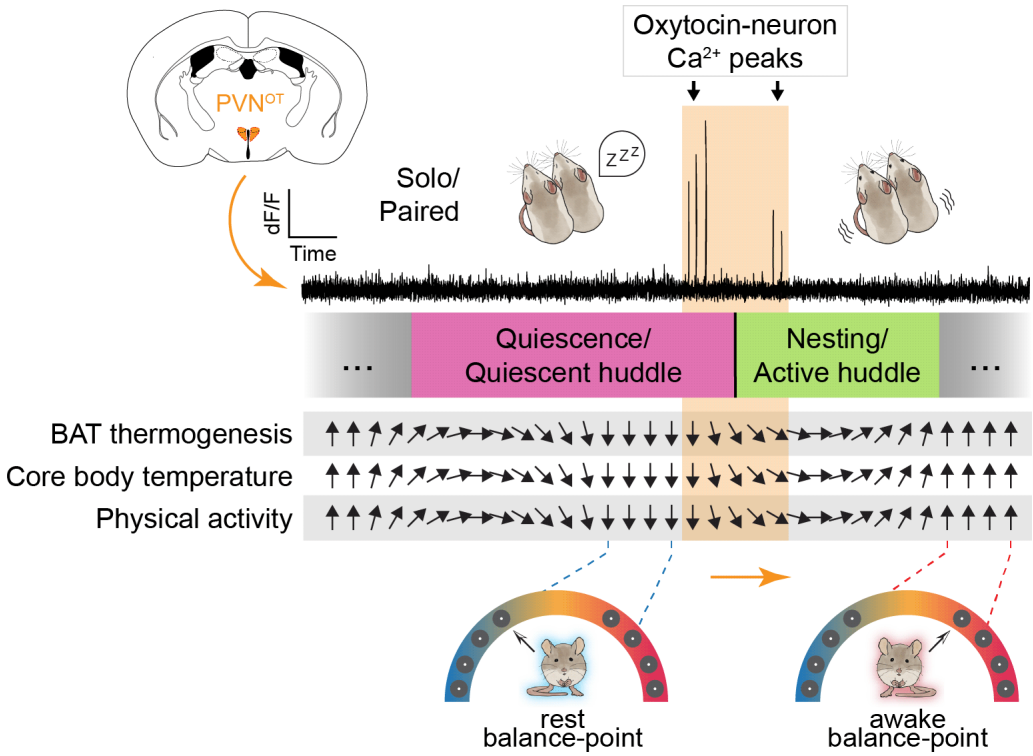

Figure 7. Graphical summary. Increased calcium activity in PVN^{OT} neurons signals the end of rest and the onset of thermogenesis and behavioral arousal. Both the frequency of large amplitude peaks and baseline calcium levels increase approximately two minutes before the end of rest (i.e., quiescence and quiescent huddle). Calcium peaks briefly continue into post-quiescent active states, like nesting and active huddling. Optogenetic stimulation of PVN^{OT} neurons during rest triggers increased BAT thermogenesis, core body temperature (Tb) and physical activity. Arrows indicate transitions between the low-Tb rest balance point (downward vertical arrows) and the high-Tb active balance point (upward vertical arrows).

Our deep-learning pipeline (SGBS) further allowed us to track thermal features (dorsal surface, brown fat, and rump) at milli-second resolution. We detected increases in BAT temperature following calcium peaks and optogenetic stimulation, supporting a role of PVN^{OT} neurons in driving state-dependent transitions towards thermogenesis. Several neural populations that promote the transition from sleep to wake have been described (Sulaman et al., 2023), some of which are directly involved in thermoregulation (Harding et al., 2019). In conjunction with another report showing that chemogenetic activation of PVN^{OT} neurons increases wakefulness (Chen et al., 2021), our data now place PVN^{OT} neurons as a key node in the initiation of thermogenic and behavioral arousal from rest. Here, we suggest a model, congruent with two other reports, whereby the transition from rest to arousal begins with a change in neural activity leading to increased thermogenesis that is either coincident with, or followed by, increased physical activity (Ootsuka et al., 2009; Škop et al., 2024) (Fig. 7). Notably, we found no evidence that decreases in PVN^{OT} activity signal transitions towards quiescence and heat loss, indicating that distinct systems drive entry to, and exit from, resting states.

Some caveats of this study should be considered. First, we did not link PVN^{OT} in vivo calcium activity or optogenetic stimulation with endocrinological release of OT. Future studies should address how the neuropeptide oxytocin (e.g., in addition to glutamate release (Hrabovszky and Liposits, 2008)) drives transitions in behavioral arousal and thermogenesis. Second, although some of our experiments were conducted with only a handful of animals, we nevertheless detected robust associations between PVN^{OT} activity and thermo-behavioral changes within individuals. Future work, incorporating more animals, could better capture variation across individuals and internal physiological states. Additionally, here we only studied females based on their

discernable thermo-behavioral states; future work could focus on determining the role of PVN^{OT} neurons in males.

Overall, these findings extend the role of in vivo PVN^{OT} neural activity dynamics beyond social behavior (Hegoburu et al., 2024; Resendez et al., 2020; Sun et al., 2025; Tang et al., 2020), parturition/lactation (Perkinson et al., 2021), maternal behavior (Carcea et al., 2021), sexual behavior (Qian et al., 2023), and stress responses (Zhan et al., 2024), and highlight their contribution to daily patterns of rest/wake transitions, thermoregulation, and energy balance. In our model PVN^{OT} neurons respond to internal physiological conditions, such as core body temperature, to coordinate autonomic and behavioral outputs necessary for adaptive thermoregulation. These insights open new directions for understanding the neural circuits that integrate social context, internal state, and metabolic demands to regulate mammalian behavior.

Acknowledgements and Funding
We thank University of Wyoming Sensory Biology Center for input; Robert Carrol for assistance with animal husbandry; members of the Nelson and Bedford laboratory for input; Sean Harrington for coding assistance; the UW Engineering Shop for designing and building hardware. This work is funded by NIH COBRE Grant 5P20GM121310-07.

Resource availability
Lead contact
For further information or requests, contact should be directed towards the lead contact, Adam Nelson (anelso74@uwyo.edu).

Materials availability
This study did not generate any new reagents.

Data and code availability
Raw data and code will be made available on a public repository.

Author contributions
M.V., J.G.L, J.F.R., N.L.B., and A.C.N. designed the study. M.V. performed the fiber photometry studies. M.V, J.G.L, and A.C.N. performed the optogenetic studies. M.V., J.G.L., B.A., C.P., and A.C.N. performed the histology studies. J.G.L, S.K. and G.J.T. performed code development. J.F.R. contributed to a previous draft of this manuscript. N.L.B. and A.C.N secured funding and provided expertise and feedback.

Declaration of Interests
The authors declare no competing interests.

References

Alberts JR. 1979. Huddling by rat pups: Group behavioral mechanisms of temperature regulation and energy conservation. *Journal of Comparative and Physiological Psychology* **92**:231. doi:10.1037/h0077459

Almeida MC, Vizin RCL, Carrettiero DC. 2015. Current understanding on the neurophysiology of behavioral thermoregulation. *Temperature* **2**:483–490. doi:10.1080/23328940.2015.1095270

Althammer F, Grinevich V. 2018. Diversity of oxytocin neurones: Beyond magno- and parvocellular cell types? *J Neuroendocrinology* **30**:e12549. doi:10.1111/jne.12549

Besnard A, Leroy F. 2022. Top-down regulation of motivated behaviors via lateral septum sub-circuits. *Mol Psychiatry* **27**:3119–3128. doi:10.1038/s41380-022-01599-3

Biag J, Huang Y, Gou L, Hintiryan H, Askarinam A, Hahn JD, Toga AW, Dong H. 2012. Cyto- and chemoarchitecture of the hypothalamic paraventricular nucleus in the C57BL/6J male mouse: A study of immunostaining and multiple fluorescent tract tracing. *J of Comparative Neurology* **520**:6–33. doi:10.1002/cne.22698

Blessing W, McAllen R, McKinley M. 2016. Control of the Cutaneous Circulation by the Central Nervous System In: Prakash YS, editor. Comprehensive Physiology. Wiley. pp. 1161–1197. doi:10.1002/cphy.c150034

Blessing W, Ootsuka Y. 2016. Timing of activities of daily life is jaggy: How episodic ultradian changes in body and brain temperature are integrated into this process. *Temperature* **3**:371–383. doi:10.1080/23328940.2016.1177159

Brownstone RM, Chopek JW. 2018. Reticulospinal Systems for Tuning Motor Commands. *Front Neural Circuits* **12**:30. doi:10.3389/fncir.2018.00030

Carcea I, Caraballo NL, Marlin BJ, Ooyama R, Riceberg JS, Mendoza Navarro JM, Opendak M, Diaz VE, Schuster L, Alvarado Torres MI, Lethin H, Ramos D, Minder J, Mendoza SL, Bair-Marshall CJ, Samadjopoulos GH, Hidema S, Falkner A, Lin D, Mar A, Wadghiri YZ, Nishimori K, Kikusui T, Mogi K, Sullivan RM, Froemke RC. 2021. Oxytocin neurons enable social transmission of maternal behaviour. *Nature* **596**:553–557. doi:10.1038/s41586-021-03814-7

Chen C-R, Zhong Y-H, Jiang S, Xu W, Xiao L, Wang Z, Qu W-M, Huang Z-L. 2021. Dysfunctions of the paraventricular hypothalamic nucleus induce hypersomnia in mice. *eLife* **10**. doi:10.7554/elife.69909

De Lecea L, Carter ME, Adamantidis A. 2012. Shining Light on Wakefulness and Arousal. *Biological Psychiatry* **71**:1046–1052. doi:10.1016/j.biopsych.2012.01.032

Endo N, Ujita W, Fujiwara M, Miyauchi H, Mishima H, Makino Y, Hashimoto L, Oyama H, Makinodan M, Nishi M, Tohyama C, Kakeyama M. 2018. Multiple animal positioning system shows that socially-reared mice influence the social proximity of isolation-reared cagemates. *Communications Biology* **1**:225. doi:10.1038/s42003-018-0213-5

Engmann AK, Bizzozzero F, Schneider MP, Pfyffer D, Imobersteg S, Schneider R, Hofer A-S, Wieckhorst M, Schwab ME. 2020. The Gigantocellular Reticular Nucleus Plays a Significant Role in Locomotor Recovery after Incomplete Spinal Cord Injury. *J Neurosci* **40**:8292–8305. doi:10.1523/JNEUROSCI.0474-20.2020

Fransson A-L, Karlsson H, Nilsson K. 2005. Temperature variation in newborn babies: importance of physical contact with the mother. *Archives of Disease in Childhood - Fetal and Neonatal Edition* **90**:F500–F504. doi:10.1136/adc.2004.066589

Froemke RC, Young LJ. 2021. Oxytocin, Neural Plasticity, and Social Behavior. *Annu Rev Neurosci* **44**:359–381. doi:10.1146/annurev-neuro-102320-102847

Fukushima A, Kataoka N, Nakamura K. 2022. An oxytocinergic neural pathway that stimulates thermogenic and cardiac sympathetic outflow. *Cell Reports* **40**:111380. doi:10.1016/j.celrep.2022.111380

Gilbert C, McCafferty D, Le Maho Y, Martrette J-M, Giroud S, Blanc S, Ancel A. 2010. One for all and all for one: the energetic benefits of huddling in endotherms. *Biological Reviews* **85**:545–569. doi:10.1111/j.1469-185X.2009.00115.x

Gordon CJ. 2012. Thermal physiology of laboratory mice: Defining thermoneutrality. *Journal of Thermal Biology* **37**:654–685. doi:10.1016/j.jtherbio.2012.08.004

Gordon CJ. 1993. Temperature Regulation in Laboratory Rodents. *Cambridge: Cambridge University Press*. doi:https://doi.org/10.1017/CBO9780511565595

Gordon CJ, Aydin C, Repasky EA, Kokolus KM, Dheyongera G, Johnstone AFM. 2014. Behaviorally mediated, warm adaptation: A physiological strategy when mice behaviorally thermoregulate. *Journal of Thermal Biology* **44**:41–46. doi:10.1016/j.jtherbio.2014.06.006

Haig D. 2008. Huddling: Brown Fat, Genomic Imprinting and the Warm Inner Glow. *Current Biology* **18**:R172–R174. doi:10.1016/j.cub.2007.12.040

Harding EC, Franks NP, Wisden W. 2020. Sleep and thermoregulation. *Current Opinion in Physiology* **15**:7–13. doi:10.1016/j.cophys.2019.11.008

Harding EC, Franks NP, Wisden W. 2019. The Temperature Dependence of Sleep. *Front Neurosci* **13**:336. doi:10.3389/fnins.2019.00336

Harshaw C, Leffel JK, Alberts JR. 2018. Oxytocin and the warm outer glow: Thermoregulatory deficits cause huddling abnormalities in oxytocin-deficient mouse pups. *Hormones and Behavior* **98**:145–158. doi:10.1016/j.yhbeh.2017.12.007

He K, Gkioxari G, Dollár P, Girshick R. 2017. Mask R-CNN. doi:10.48550/ARXIV.1703.06870

Hegoburu C, Tang Y, Niu R, Ghosh S, Triana Del Rio R, De Araujo Salgado I, Abatis M, Alexandre Mota Caseiro D, Van Den Burg EH, Grundschober C, Stoop R. 2024. Social buffering in rats reduces fear by oxytocin triggering sustained changes in central amygdala neuronal activity. *Nat Commun* **15**. doi:10.1038/s41467-024-45626-z

Hrabovszky E, Liposits Z. 2008. Novel Aspects of Glutamatergic Signalling in the Neuroendocrine System. *J Neuroendocrinology* **20**:743–751. doi:10.1111/j.1365-2826.2008.01719.x

Johnson ZV, Revis AA, Burdick MA, Rhodes JS. 2010. A similar pattern of neuronal Fos activation in 10 brain regions following exposure to reward- or aversion-associated contextual cues in mice. *Physiology & Behavior* **99**:412–418. doi:10.1016/j.physbeh.2009.12.013

Jung S, Lee M, Kim D-Y, Son C, Ahn BH, Heo G, Park J, Kim M, Park H-E, Koo D-J, Park JH, Lee JW, Choe HK, Kim S-Y. 1998. A forebrain neural substrate for behavioral thermoregulation. *Neuron* **110**:266-279.e9. doi:10.1016/j.neuron.2021.09.039

Kasahara Y, Sato K, Takayanagi Y, Mizukami H, Ozawa K, Hidema S, So K-H, Kawada T, Inoue N, Ikeda I, Roh S-G, Itoi K, Nishimori K. 2013. Oxytocin Receptor in the Hypothalamus Is Sufficient to Rescue Normal Thermoregulatory Function in Male Oxytocin Receptor Knockout Mice. *Endocrinology* **154**:4305–4315. doi:10.1210/en.2012-2206

Landen JG, Vandendoren M, Killmer S, Bedford NL, Nelson AC. 2024. Huddling substates in mice facilitate dynamic changes in body temperature and are modulated by Shank3b and Trpm8 mutation. *Communications Biology* **7**:1186. doi:10.1038/s42003-024-06781-7

Li H, Jiang T, An S, Xu M, Gou L, Ren B, Shi X, Wang X, Yan J, Yuan J, Xu X, Wu Q-F, Luo Q, Gong H, Bian W-J, Li A, Yu X. 2024. Single-neuron projectomes of mouse paraventricular hypothalamic nucleus oxytocin neurons reveal mutually exclusive projection patterns. *Neuron* **112**:1081-1099.e7. doi:10.1016/j.neuron.2023.12.022

Maloney SK, Fuller A, Mitchell D, Gordon C, Overton JM. 2014. Translating Animal Model Research: Does It Matter That Our Rodents Are Cold? *Physiology* **29**:413–420. doi:10.1152/physiol.00029.2014

Mathis A, Mamidanna P, Cury KM, Abe T, Murthy VN, Mathis MW, Bethge M. 2018. DeepLabCut: markerless pose estimation of user-defined body parts with deep learning. *Nat Neurosci* **21**:1281–1289. doi:10.1038/s41593-018-0209-y

Menon R, Süß T, Oliveira VEDM, Neumann ID, Bludau A. 2022. Neurobiology of the lateral septum: regulation of social behavior. *Trends in Neurosciences* **45**:27–40. doi:10.1016/j.tins.2021.10.010

Morrison S F. 2011. Central neural pathways for thermoregulation. *Front Biosci* **16**:74. doi:10.2741/3677

Morrison SF, Madden CJ, Tupone D. 2014. Central Neural Regulation of Brown Adipose Tissue Thermogenesis and Energy Expenditure. *Cell Metabolism* **19**:741–756. doi:10.1016/j.cmet.2014.02.007

Morrison SF, Nakamura K. 2019. Central Mechanisms for Thermoregulation. *Annu Rev Physiol* **81**:285–308. doi:10.1146/annurev-physiol-020518-114546

Nixdorf-Miller A, Hunsaker DM, Hunsaker Iii JC. 2006. Hypothermia and Hyperthermia Medicolegal Investigation of Morbidity and Mortality From Exposure to Environmental Temperature Extremes. *Archives of Pathology & Laboratory Medicine* **130**:1297–1304. doi:10.5858/2006-130-1297-HAHMIO

Noble EE, Billington CJ, Kotz CM, Wang C. 2014. Oxytocin in the ventromedial hypothalamic nucleus reduces feeding and acutely increases energy expenditure. *American Journal of Physiology-Regulatory, Integrative and Comparative Physiology* **307**:R737–R745. doi:10.1152/ajpregu.00118.2014

Ootsuka Y, de Menezes RC, Zaretsky DV, Alimoradian A, Hunt J, Stefanidis A, Oldfield BJ, Blessing WW. 2009. Brown adipose tissue thermogenesis heats brain and body as part of the brain-coordinated ultradian basic rest-activity cycle. *Neuroscience* **164**:849–861. doi:10.1016/j.neuroscience.2009.08.013

Perkinson MR, Kim JS, Iremonger KJ, Brown CH. 2021. Visualising oxytocin neurone activity in vivo: The key to unlocking central regulation of parturition and lactation. *J Neuroendocrinology* **33**. doi:10.1111/jne.13012

Qian T, Wang H, Wang P, Geng L, Mei L, Osakada T, Wang L, Tang Y, Kania A, Grinevich V, Stoop R, Lin D, Luo M, Li Y. 2023. A genetically encoded sensor measures temporal oxytocin release from different neuronal compartments. *Nat Biotechnol* **41**:944–957. doi:10.1038/s41587-022-01561-2

Refinetti R. 2020. Circadian rhythmicity of body temperature and metabolism. *Temperature* **7**:321–362. doi:10.1080/23328940.2020.1743605

Refinetti R. 1999. Relationship between the daily rhythms of locomotor activity and body temperature in eight mammalian species. *American Journal of Physiology-Regulatory, Integrative and Comparative Physiology* **277**:R1493–R1500. doi:10.1152/ajpregu.1999.277.5.R1493

Resendez SL, Namboodiri VMK, Otis JM, Eckman LEH, Rodriguez-Romaguera J, Ung RL, Basiri ML, Kosyk O, Rossi MA, Dichter GS, Stuber GD. 2020. Social Stimuli Induce Activation of Oxytocin Neurons Within the Paraventricular Nucleus of the Hypothalamus to Promote Social Behavior in Male Mice. *J Neurosci* **40**:2282. doi:10.1523/JNEUROSCI.1515-18.2020

Rizzi-Wise CA, Wang DV. 2021. Putting Together Pieces of the Lateral Septum: Multifaceted Functions and Its Neural Pathways. *eNeuro* **8**:ENEURO.0315-21.2021. doi:10.1523/ENEURO.0315-21.2021

Rogers JF, Vandendoren M, Prather JF, Landen JG, Bedford NL, Nelson AC. 2024. Neural Cell-types and Circuits Linking Thermoregulation and Social Behavior. *Neuroscience & Biobehavioral Reviews* 105667. doi:10.1016/j.neubiorev.2024.105667

Romanovsky AA. 2018. The thermoregulation system and how it worksHandbook of Clinical Neurology. Elsevier. pp. 3–43. doi:10.1016/B978-0-444-63912-7.00001-1

Seoyoung Son, Steffy B. Manjila, Kyra T. Newmaster, Yuan-ting Wu, Daniel J. Vanselow, Matt Ciarletta, Todd E. Anthony, Keith C. Cheng, Yongsoo Kim. 2022. Whole-Brain Wiring Diagram of Oxytocin System in Adult Mice. *J Neurosci* **42**:5021. doi:10.1523/JNEUROSCI.0307-22.2022

Škop V, Guo J, Liu N, Xiao C, Hall KD, Gavrilova O, Reitman ML. 2020. Mouse Thermoregulation: Introducing the Concept of the Thermoneutral Point. *Cell Reports* **31**:107501. doi:10.1016/j.celrep.2020.03.065

Škop V, Liu N, Xiao C, Stinson E, Chen KY, Hall KD, Piaggi P, Gavrilova O, Reitman ML. 2024. Beyond day and night: The importance of ultradian rhythms in mouse physiology. *Molecular Metabolism* **84**:101946. doi:10.1016/j.molmet.2024.101946

Škop V, Xiao C, Liu N, Gavrilova O, Reitman ML. 2021. The effects of housing density on mouse thermal physiology depend on sex and ambient temperature. *Molecular Metabolism* **53**:101332. doi:10.1016/j.molmet.2021.101332

Sotelo MI, Markunas C, Kudlak T, Kohtz C, Vyssotski AL, Rothschild G, Eban-Rothschild A. 2024. Neurophysiological and behavioral synchronization in group-living and sleeping mice. *Current Biology* **34**:132-146.e5. doi:10.1016/j.cub.2023.11.065

Sotelo MI, Tyan J, Markunas C, Sulaman BA, Horwitz L, Lee H, Morrow JG, Rothschild G, Duan B, Eban-Rothschild A. 2022. Lateral hypothalamic neuronal ensembles regulate pre-sleep nest-building behavior. *Current Biology* **32**:806-822.e7. doi:10.1016/j.cub.2021.12.053

Sulaman BA, Wang S, Tyan J, Eban-Rothschild A. 2023. Neuro-orchestration of sleep and wakefulness. *Nat Neurosci* **26**:196–212. doi:10.1038/s41593-022-01236-w

Sun W, Zhang G-W, Huang JJ, Tao C, Seo MB, Tao HW, Zhang LI. 2025. Reviving-like prosocial behavior in response to unconscious or dead conspecifics in rodents. *Science* **387**:eadq2677. doi:10.1126/science.adq2677

Sutton AK, Pei H, Burnett KH, Myers MG, Rhodes CJ, Olson DP. 2014. Control of Food Intake and Energy Expenditure by Nos1 Neurons of the Paraventricular Hypothalamus. *J Neurosci* **34**:15306–15318. doi:10.1523/JNEUROSCI.0226-14.2014

Tan CL, Knight ZA. 2018. Regulation of Body Temperature by the Nervous System. *Neuron* **98**:31–48. doi:10.1016/j.neuron.2018.02.022

Tang Y, Benusiglio D, Lefevre A, Hilfiger L, Althammer F, Bludau A, Hagiwara D, Baudon A, Darbon P, Schimmer J, Kirchner MK, Roy RK, Wang S, Eliava M, Wagner S, Oberhuber M, Conzelmann KK, Schwarz M, Stern JE, Leng G, Neumann ID, Charlet A, Grinevich V. 2020. Social touch promotes interfemale communication via activation of parvocellular oxytocin neurons. *Nature Neuroscience* **23**:1125–1137. doi:10.1038/s41593-020-0674-y

TorchVision maintainers and contributors. 2016. TorchVision: PyTorch's Computer Vision library.

Yaguchi K, Hagihara M, Konno A, Hirai H, Yukinaga H, Miyamichi K. 2023. Dynamic modulation of pulsatile activities of oxytocin neurons in lactating wild-type mice. *PLoS ONE* **18**:e0285589. doi:10.1371/journal.pone.0285589

Yaguchi K, Miyamichi K, Tasaka G. 2024. Flexible adjustment of oxytocin neuron activity in mouse dams revealed by microendoscopy. *Sci Adv* **10**. doi:10.1126/sciadv.adt1555

Yukinaga H, Hagihara M, Tsujimoto K, Chiang H-L, Kato S, Kobayashi K, Miyamichi K. 2022. Recording and manipulation of the maternal oxytocin neural activities in mice. *Current Biology* **32**:3821-3829.e6. doi:10.1016/j.cub.2022.06.083

Yukinaga H, Miyamichi K. 2025. Oxytocin and neuroscience of lactation: Insights from the molecular genetic approach. *Neuroscience Research* S0168010225000124. doi:10.1016/j.neures.2025.01.002

Zhan S, Qi Z, Cai F, Gao Z, Xie J, Hu J. 2024. Oxytocin neurons mediate stress-induced social memory impairment. *Current Biology* **34**:36-45.e4. doi:10.1016/j.cub.2023.11.037

Zhang Y, Rózsa M, Liang Y, Bushey D, Wei Z, Zheng J, Reep D, Broussard GJ, Tsang A, Tsegaye G, Narayan S, Obara CJ, Lim J-X, Patel R, Zhang R, Ahrens MB, Turner GC, Wang SS-H, Korff WL, Schreiter ER, Svoboda K, Hasseman JP, Kolb I, Looger LL. 2023. Fast and sensitive GCaMP calcium indicators for imaging neural populations. *Nature* **615**:884–891. doi:10.1038/s41586-023-05828-9

METHODS

Animals

OT and FOS histology. C57B6/J (Strain #: 000664) female mice were purchased from Jackson Laboratory and were 8 to 11 weeks old during the experimental period. Virgin, group-housed females were used for all trials unless otherwise specified.

PVN^{OT} manipulation and recording. Oxytocin-Ires-Cre mice were purchased from Jackson Laboratory (Strain #: 024234) (Wu et al., 2012). Animals were bred and maintained at the University of Wyoming. Experimental female mice ranged from 9-20 weeks old during the experimental period. All experimental mice were group-housed with *ad libitum* access to food and water in a room maintained at 23±2°C with a standard 12 h light / dark cycle (light: 6:00-18:00; dark: 18:00-6:00) until they were used for surgery or experiments. Animals were housed in Optimice® IVC cage systems; cages were enriched with red huts, nestlets, and a mix of cob and pine bedding. Mice used were 18-26g during the experimental period. Animal genotyping was outsourced to Transnetyx using ear tissue biopsies. All procedures were approved by the University of Wyoming Institute Animal Care and Use Committee (IACUC) in compliance with NIH guidelines for the care and use of laboratory animals.

FOS/*Fos* behavior assays

To measure FOS protein expression across brain regions, mice were placed into the home cage recording suite as described (Landen et al., 2024) for at least 24 hours prior to behavior being monitored, with the cage's camera being connected to a Zoom meeting. After the 24 hours, beginning at the start of the light cycle when huddling is most frequent, a human observer monitored behavior from another room, without interrupting natural behavior. Once the target behavior was observed for a minimum of 15 consecutive minutes, 90 minutes were counted from the onset of the behavior, and animals were pulled from the recording suite for histology.

To determine *Fos* transcription in PVN^{OT} neurons during different huddling states, C57B6/J female mice that were 10 weeks old were housed in home cages in trios. Mice were habituated to the conditions, handling, and the cage lid camera set up for ~5 days prior to recording. Animals were split into two groups: active huddle (N=6) and quiescent huddle (N=3). To capture active huddle *Fos* transcription, mice were recorded using the cage lid camera connected to a Zoom meeting. The time of active huddle onset was documented, and mice were sacrificed 30 minutes later. To determine quiescent huddle *Fos* transcription, mice were recorded as described above. Mice were sacrificed 30 minutes after the onset of quiescent or active huddle. All brains were dissected, embedded in OCT (Fisher Scientific, #23-730-571) and stored in -80°C.

Animal Surgery

Pre- and post-surgical procedures. Prior to surgery, animals were given an analgesic dose of carprofen (20 mg/kg, s.c.). Mice were deeply anesthetized using a mixture of ketamine and xylazine (100 mg/kg and 10 mg/kg, respectively, administered i.p.). Post-surgery, the mice were returned to a warm and clean home cage. For post-operative care, antibiotic ointment (Neomycin and Polymyxin B Sulfates and Dexamethasone Ophthalmic Ointment, Bausch + Lomb) was topically applied to the incision, animals received 20 mL/Kg of lactated ringer's solution s.c., and closely observed until active. Upon emergence from anesthesia, 1 mg/kg of buprenorphine extended-release solution was administered subcutaneously between the shoulder blades. Animals were housed with cagemates and monitored daily. Carprofen was administered for three days post-surgery.

Temperature logger implants. To continuously measure internal body temperature, laparotomies were performed to implant mice with Star-Oddi DST nano-T temperature loggers. The loggers were

sterilized with glutaraldehyde and rinsed with sterile PBS prior to being implanted. Mice received pre-operative care and were anesthetized as described above. A one-centimeter incision was made in the skin and underlying peritoneum, and the temperature logger was placed into the abdominal cavity. The peritoneum was sutured with PGA absorbable sutures, while the skin was closed with nylon (nonabsorbable) sutures. Mice received post-surgical care as described above.

Stereotaxic GCaMP injections and fiber implants. For fiber photometry recordings, oxytocin-Ires-Cre heterozygous, pair-housed, female mice at 8-12 weeks of age underwent stereotaxic surgery in which pGP-AAV9-syn-FLEX-jGCaMP8s-WPRE (#162377, Addgene, titer: 2.7 x 10^{13} gc/mL) was delivered to the PVN. Mice were head-fixed on a digital mouse stereotax (Stoelting, 51730D). For added analgesia, a local anesthetic (5% lidocaine) was delivered subcutaneously along the incision site before cutting. A midline incision was made along the top of the skull, the periosteum was cleared with 3% hydrogen peroxide, and the skull was dried off with canned air. Vertical measurements of bregma and lambda were taken and aligned to the same plane (DV of ± 0.05 mm). The AAV was delivered using a programmable nanoliter injector, (Nanoject III, Drummond Scientific) (300nL per side: 6 cycles of 50nL delivered at 2nL/s with 10 second delays). To allow for proper diffusion of solution into brain tissue, the needle was left in for 10 minutes before retracting. PVN coordinates relative to bregma and DV measured from the top of the brain: AP = -0.76mm, ML= ±0.19mm, DV= -4.62mm.
A fiber-optic cannula (Ø1.25mm ferrule, Ø200 µm core, NA = 0.37, L= 6.5 mm, Neurophotometrics Ltd.) was then lowered into the injection site until the tip was located ~ 0.02 mm above the viral injection. The cannula was anchored in place with dental cement (C&B Metabond) such that a dome-shaped cap was halfway up the black ceramic ferrule and covered the entire incision. Post-operative care and recovery took place as described above. Two weeks post recovery, animals were tested for GCaMP signal using the Neurophotometrics photometry system (as described in "**Fiber photometry recordings"**). If a signal was detected, animals underwent a laparotomy to implant a temperature logger as described above. Animals with no detectable signal were excluded from recordings.

ChR2 injection & optic fiber implant. For optogenetic stimulation of PVN^{OT} neurons, Oxytocin-Ires-Cre heterozygous, pair-housed, female mice at 8-12 weeks of age were split into two different groups: ChR2+ and control (ChR2-) animals. ChR2+ animals underwent stereotaxic injections with AAVDJ-EF1a-DIO-hChR2(H134R)-EYFP-WPRE-pA (Salk, titer: 4.03x10^{13} gc/mL) using the stereotaxic surgical procedure described above. Viral vectors were delivered using a programmable nanoliter injector, (Nanoject III, Drummond Scientific) (200nL per side: 4 cycles of 50nL delivered at 1nL/s with 10 second delays). Both ChR2+ and control animals were implanted with a fiber optic cannula (Ø1.25mm ferrule, Ø200 µm core, NA = 0.37, L= 6.5 mm, Neurophotometrics Ltd.). All optogenetic animals were given a minimum of seven days to recover before undergoing a laparotomy to implant a temperature logger.

Stereotaxic DREADD, CTB and tail vein injections. To identify PVN^{OT} projections to rMR, a subset of mice received two stereotaxic injections: one of AAV5-hSyn-DIO-hM3D(Gq)-mCherry (#44361, Addgene, titer: 2.6 x 10^{13} gc/mL) in the PVN and one of cholera toxin subunit B conjugated with Alexa Fluor 647 (Invitrogen, C34778). Using the same surgical procedure and PVN coordinates as mentioned above, 300 nL of AAV was delivered per side (6 cycles of 50nL delivered at 2nL/s with 10 second delays). The incision was closed using absorbable PGA suture threads and antibiotic ointment was applied topically along the incision. Animals recovered for two weeks to maximize viral expression. A second stereotaxic surgery was performed to deliver a volume of 10 nL of 0.5% CTB into the rMR. RMR coordinates relative to bregma and DV measured from the top of the brain: AP = -5.80mm, ML= 0.00mm, DV= -4.95mm. Mice received post-operative care as described above and recovered for 3-4 days. For intravenous labeling of magnocellular and parvocellular OT neurons, mice received 15 uL of 4% Fluoro-Gold (Fluorochrome) diluted in 100 uL of sterile saline. Prior to injection, mice were given an analgesic dose of carprofen (20 mg/kg, s.c.). Mice were briefly restrained using a modified 50 mL conical tube, in which holes were drilled to allow for proper air flow and respiration. Mouse tails were

interposed between two heating pads to enhance visibility of the tail vein. Tails were wiped down with 70% ethanol and FG was administered via either right or left lateral tail vein using a 0.5 mL 28G syringe. Mice were sacrificed 24- 48 hours post-FG administration.

Histology

FOS Immunohistochemistry. For quantitative analysis of FOS expression, mice were given a lethal dose of isoflurane after removal from the home cage recording suite. Animals were then transcardially perfused with 1X PBS and 4% paraformaldehyde (PFA) in PBS. Brains were removed and kept in 4% PFA overnight at 4°C. Brains were sliced into 60 um sections using a vibratome (Leica VT1000S) and every other slice was saved in 48-well plates, wrapped in parafilm in 1X PBS, overnight at 4°C. The next day, 0.3 mL of block solution (0.20% triton, 10% natural goat serum (NGS) (Jackson ImmunoResearch 005-000-121), in 1X PBS) was placed into each well and incubated for one hour at room temperature on a plate shaker. Block was removed and replaced with freshly made primary antibody solution (c-Fos (9F6) Rabbit mAb, Cell Signaling, 14609, 1:1000 dilution in block solution) and incubated for 48 hours on a shaker at 4°C. Slices were washed three times with 1X PBS for 15 minutes. Slices were then incubated in secondary antibody solution (Goat anti-Rabbit IgG, Alexa Fluor Plus 555, Thermo Scientific, A32732, 1:500 dilution in block) for 2 hours on a shaker at room temperature and protected from light. Wash steps were repeated with 1X PBS. Slices were then mounted on Superfrost Plus slides using a paintbrush and stained with DAPI mounting medium (Vectashield H-2000). Slides were imaged with a Zeiss Axio Scan.Z1 fluorescent microscope. Regions were identified by finding all locations that displayed FOS expression and cropped using ImageJ alongside the Allen Brain Atlas. The quantity of cells and overlap was calculated using a custom CellProfiler 4.2.1 script.

Fluorescent *in situ* hybridization (RNAscope). For quantitative analysis of *Oxt* and *Fos* overlap in PVN^{OT} mice were anesthetized with a lethal amount of isoflurane. Brains were extracted, embedded in OCT and stored at -80°C. Brains were sectioned at 16 µm using a cryostat and subsequently stored at -80°C. For *in situ, s*lides containing brain sections were placed in 4% PFA for 45 minutes and then were dehydrated in 50%, 70% and 100% ethanol for 5 minutes each at RT. Slides dried for 5 minutes after dehydration and hydrogen peroxide was added for 10 minutes at RT. Slides were then treated with Protease III for 30 minutes at RT to allow for antigen accessibility. The probe cocktail contained *Oxt* (ACD Bio, #493171) and *Fos* (ACD Bio, #316921) and was diluted at 1:2 ratio with probe diluent. An aliquot of 40µL of probe cocktail was added to each section and incubated in a 40°C oven for two hours. For amplification, 40µL of AMP 1 was added each slice and placed in the 40°C oven for 15 minutes. AMP 2 was then added to each slice and slides were again incubated at 40°C for 15 minutes. Finally, 2-3 drops of AMP 3 were added to each slice and slides were incubated at 40°C for 30 minutes.

Fluorophores were added to each channel and diluted at 1:1500. Each fluorophore was added by first opening the channel using 2-3 drops of HRP on each slice and incubating at 40°C for 15 minutes. The fluorophore was added at a volume of 40 µL to each slice and slides were incubated at 40°C for 30 minutes. To close the channel, 2-3 drops of blocker were added to each slice and incubated for 15 minutes. Lastly, a drop of DAPI (ACD Bio, #320858**)** was added to each slice for 30-45 seconds. DAPI was allowed to dry for approximately 3 minutes before immediately coverslipping with 1-2 drops of ProLong Gold (Invitrogen, P36930). Slides were protected from any surrounding light, left to dry overnight and imaged with a Zeiss Axio Scan.Z1.

AAV expression. To verify AAV injection sites, animals who had received stereotaxic DREADD, GCaMP8s, or CHR2 injections were sacrificed at ≤18 weeks. Mice were deeply anesthetized with a lethal amount of isoflurane and perfused with 4% PFA. Extracted brains were then stored in 4% PFA overnight at 4°C before being sliced at 60 µm using a vibratome (Leica VT1000S). PVN regions were identified via the Allen Brain Atlas. PVN slices were stained with a DAPI mounting medium (200

µl/slide, Vectashield H-2000) and scanned using a Zeiss Axio Scan.Z1. Images were enhanced and/or pseudo-colored using ImageJ.

Fiber photometry recordings

Recording setup. The Neurophotometrics fiber photometry system (FP3001), operating with Bonsai (Version 2.72) software, was used to acquire photometric data with concurrent video recordings (Arducam, OV9281). Patchcords (MBF Bioscience, NPM-BPC-4) were attached to the fiber ferrules, and held in place by either ceramic sleeves or by a quick-release interconnecter (ThorLabs, ADAL3). Calcium dependent GCaMP fluorescence signals were recorded with light from a 470-nm LED that was band-pass filtered, narrowed with a collimator, reflected by a dichroic mirror, and focused on the sensor of a CCD camera by a 20x objective. To account for auto-fluorescence and possible motion artifacts, a 415-nm LED for calcium-independent isosbestic fluorescence signal was used. The recorded signals were acquired with a sampling rate of 30 Hz for each channel at 100% duty cycle. LED light power was calibrated prior to every recording using a power meter (ThorLabs, PM100USB and S120C). LED light was delivered at a power that resulted in 60µW of 415-nm light, and 85 µW of 470-nm light at the tip of the patchcord.

Recording conditions. Photometric recordings occurred in the home cage, with the cage-lid replaced by a custom-fit metal sleeve that extended the cage wall height to 16". Optic fiber-implanted mice and their pair-housed sister were habituated to the connector and patchcord prior to commencement of experimental schedule. Habituation periods ranged from several days to a week depending on individual animal reaction to the patchcord and to sufficiently aversion train the cagemate. Aversion training was performed during habituation periods by lightly coating the patchcord with diluted capsaicin (EMD Millipore, 211275). The cagemate and implant mouse were observed, and training was repeated until the cagemate associated the unpleasant sensation of capsaicin with chewing of the patchcord. Recordings were approximately 2-hours and were conducted at three different floor temperatures (15Cº, 23Cº and 29ºC), with and without the sister cage-mate. Floor temperature was controlled by placing the home-cage onto a custom aluminum chassis that attached to the Hot/Cold Plate (Ugo Basile, 35300), temperature was then validated by a temperature logging iButton (DS1922L-F5, Embedded Data Systems) placed inside the home-cage. A portion of the nesting material was removed before experiments to prevent occlusion of the animals during the recording (see Supplementary Video 1 for typical amount of bedding left in cage).

Validation trials. To verify the bursting activity of PVN oxytocin neurons observed in photometry recordings, virgin females were crossed with stud males after completing at least two photometry trials (as described above). The dams and pups were housed in their home cages throughout the trial period. Dams were recorded during nursing and lactation. Maternal oxytocin neural activity was recorded at the following timepoints: postpartum day (PPD) 2, 5, 7, 8, 9, and 14. For this experiment the minimum peak amplitude was set to be > 7 standard deviations (sds) above the mean. This threshold was obtained by examining peaks in mothers that clearly displayed pulsatile activity bursts during lactation and closely resembled the peak dynamics that have been previously described during lactation (Two REFS).

Behavioral characterization. Videos were uploaded to Noldus Ethovision XT 16, where the physical activity of the mice (calculated total percentage of pixel change between frames) and behaviors were identified. Activity in the paired context was defined as the summed activity for both animals.
The behaviors for solo photometry animals were manually scored as follows: Locomotor Activity (LMA), Eating or Drinking (EaDr), Grooming (Groom), Nesting or Nest Building Nest (Nest) where the animal engaged in nest-building behavior or activity within its nest other than grooming, Quiescence (Quies) where the animal is inactive inside its nest, and Stationary (Sta) which was defined as animal inactivity outside of the nest.

The behavior of the photometry animal for paired assays was manually scored as follows: Locomotor Activity (LMA), Eating or Drinking (EaDr), contact initiated (ConI), contact received (ConR), Grooming (Groom), Nesting or Building Nest (Nest) characterized by the photometry animal engaging in nest-building behavior or its activity inside the nest while its cagemate engaged in nest-building behavior, Active huddle (AHud) defined as physical contact and activity between both animals in the nest, Quiescent Huddle (QHud) referred to physical contact and inactivity between both animals in the nest, Quiescence (Quies) where the photometry animal was engaging in inactivity alone in the nest, and Stationary (Sta).
Behavior and activity data was exported at 10 frames per second as a .csv file and imported to R for analysis.

Calcium data preprocessing. Fluorescent signal data preprocessing was done with a custom R script as follows: 415 and 470 channels de-interleaved; 470 channel filtered to remove high-frequency noise using a 4th-order Butterworth filter (Van Boxtel et al., 2021) modified to remove end-effect transients; trimmed to remove approximately the first six minutes of data (to mitigate the effect of photobleaching); if necessary, further trimmed to remove effects of disruptions to the patchcord (chewing or twisting); smoothed with a sliding window function (rollapply; width = 9) (Zeileis et al., 2004).
To correct the calcium-dependent signal from effects of photobleaching and heat-mediated LED decay, we first extracted the "fitted values" from the linear relationship between the 470 (calcium-dependent) and 415 (calcium independent) fluorescent signals. Next, to calculate dF/F we divided the 470 signal by these fitted values. Because we observed occasional artifactual shifts in baseline dF/F values, we baseline corrected dF/F using the iterative least squares method (Liland and Mevik, 2011). The Z-scored dF/F was calculated as $Z = (\chi - \mu)/ \sigma$, where μ is the mean dF/F and σ is the standard deviation of dF/F. To define peaks, we used the findpeaks function (Borchers, 2011), with the minimum peak distance set at two seconds and the minimum peak height set at six standard deviations above the mean dF/F. Photometric data were aligned to behavioral data (exported from Noldus Ethovision) and Tb data (exported from Mercury) using common centisecond-resolution timestamps and reduced to a sampling frequency of 10 frames per second.

Peri-event data oriented on specific events (i.e., calcium peaks or start/stop frames of behavioral bouts) were extracted using a custom function that (1) extracts the indices of the events and (2) generates a list of vectors for a specified number of rows before and after the event.
To compare longitudinal physiological patterns of activity in PVN^{OT} neurons in virgin females (primary subjects of this study) compared to nursing and lactation, we made the following modifications to the protocol as described above. First, to quantify PVN^{OT} peak characteristics (amplitude, full width half maximum, interpeak interval) before linear normalization and baseline correction, (i.e., to better describe the dynamics of their native characteristics), we corrected the calcium-dependent signal from effects of photobleaching and heat-mediated LED decay using an exponential decay model. Specifically, we used a self-starting nls (nonlinear least squares) function in R to fit the isosbestic data with the following model: y(t) ~ SSasymp(timeS, yf, y0, log_alpha), where the measured isosbestic value y starts at y0 and decays towards yf at a rate α. SSasymp is a shortcut that guesses its own parameters; instead of fitting the rate constant α directly, it searches for the logarithm of α: y(t)~yf+(y0−yf)e^−exp(logα)t. We then linearly scale this fitted decay to the calcium-dependent data using robust regression (MASS::rlm with the psi function set to bisquare); finally, we divided the calcium-dependent data by this scaled fit to get a corrected signal.
In accordance with previous work, we examined three epochs in the same animals: virgin females; early-stage lactation (PPD 2-7); and late-stage lactation (PPD 8-14). To calculate the full-width half maximum (FWHM) of PVN^{OT} peaks, we used a custom function that performs the following steps: finds each peak; determines the half-max value; interpolates where the signal crosses the half-max value; computes the FWHM as the difference between these crossing points. To calculate the interpeak interval (IPI), we used the lead function in R to compute the time (in seconds) from one peak to the next on a per-recording basis.

Computer vision analysis

Processing Flir .seq files. RGB videos, timestamps, and thermal data were extracted from Flir thermographic .seq files using a Python-based adaptation of *ThermImageJ* [3]. Raw images were obtained via Flirpy [4], converted to RGB, and merged into AVI video files. Metadata, including timestamps and frame rates, was extracted using *Exiftool* [5]. This workflow provided thermal images for model training, AVI videos for analysis, and timestamps and temperature data for integration with behavioral information. The processing script is available at https://github.com/j-landen/seq_process.

Custom Mask R-CNN for body part segmentation. To extract surface temperature from thermographic videos, we developed a computer vision pipeline (*SGBS*) integrating keypoints from DeepLabCut [6] with a custom Mask R-CNN [7] model for segmenting specific body regions. A DeepLabCut deep learning model was first trained on manually labeled data from 1800 images to detect ten keypoints along the dorsal surface of the mice (nose, implant, head tip, neck base, center back, tail base, mid tail, patchcord, and right & left shoulder). These keypoints were then incorporated into an attention layer alongside the thermal images to enhance texture representation and improve segmentation accuracy. The custom Mask R-CNN was trained using 457 images on *Darwin* (V7 Labs) to segment the BAT region, the rump region, and the entire dorsal surface of the mouse. Finally, segmented regions were mapped to their corresponding pixel-wise temperature data, providing per-frame temperature measurements (mean, min, max, SD) for each target region. The *SGBS* code is available at: https://github.com/j-landen/SGBS.

To determine the efficacy of the custom segmentation software, it was compared with an unmodified Mask R-CNN model, using the same pre-trained weights (*ResNet50_Weights IMAGENET1K_V2*) and the same 450 manually-trained images (80% training, 20% validation). Both models ran over 200 epochs, and loss was measured after each epoch. Loss is calculated as the sum of three components: (1) a classification loss (cross-entropy) that assesses how accurately each body part is identified, (2) a bounding box regression loss that measures how close the predicted box is to the ground truth, and (3) a mask loss (binary cross-entropy) that evaluates pixel-by-pixel agreement between the predicted mask and the ground truth mask [7,8].

Optogenetic stimulation

Recording setup. Blue light (450 nm) stimulation was delivered using the Neurophotometrics fiber photometry system (FP3001), with simultaneous video and thermal recording. Mono-filament patchcords (Doric Lenses, MFP_200/220/900-0.37_3m_FC-MF1.25) were attached to the fiber ferrules and held in place by a quick-release interconnecter (ThorLabs, ADAL3). Optogenetic laser power was measured prior to every recording using a power meter (ThorLabs, PM100USB and S120C). Optogenetic activation used a frequency of 10 Hz, with a 20 ms pulse width (20% duty cycle) and 10 mW of power measured at the tip for either 10- or 20-second trains.

Optogenetic recordings occurred in the home cage, with the same setup as fiber photometry recordings, described above. Mice were pair-housed until recording. One animal was tested at a time, while the other animal was placed in a holding cage for the duration of the experiment. During experiments, animals were observed remotely from a different room. The human observer turned on blue light stimulation after the animal had been inactive for a minimum of two minutes. Stimulations were a minimum of ten minutes apart from one another. Experiments were two hours long, averaging four to seven stimulations. Every animal was tested at least twice using each stimulation time (10s and 20s), until a minimum of 10 total stimulations occurred per animal, per stimulation time.

Optogenetic data preprocessing. For each stimulation, data spanning 5 min (–300 s) before to 10 min (+600 s) after light onset were extracted, with the onset designated as time 0. Core body

temperature (Tb) data was recorded once every five seconds for the duration of the experiment. We therefore subset all other data to the same rate for core Tb analyses.

Activity levels were measured at a rate of 10 Hz, so all data were subset to the same rate for activity analyses. As activity is measured using percent pixel movement over the entire image, activity was first set to a logarithmic scale, to measure small differences in change, then normalized using a Z score across mouse IDs to account for differences in baseline activity levels.

Feature-specific surface temperatures using SGBS were measured at a rate of around 20-30 Hz, depending on the Flir A50's output. As previously described, all surface temperature data was subset to 10 Hz and aligned to surface temperature data based on the nearest timestamps when the laser was turned on (< 0.1s deviation). To eliminate the effect of outliers originating from an incorrect segmentation output, all surface temperature data were smoothed with a rolling average over one half of a second. To eliminate differences in baselines per animal, every value was baseline-normalized using $\Delta T/T$, where each temperature value was expressed as a change from the pre-stimulation mean (3-minutes prior to light on) relative to that baseline.

To assess whether optogenetic effects varied with initial thermal state, core body temperature at the onset of each blue-light pulse (Tb-T0) was recorded. Because Tb-T0 values were generally higher than those observed during spontaneous PVNOT calcium peaks, stimulations were stratified for each mouse into "low Tb-T0" and "high Tb-T0" trials using that animal's mean Tb-T0 as the cutoff. The two strata were then analyzed separately.

Statistics

Statistical results are reported in Table S1.

Effect of behavior state on FOS expression. To determine the effect of behavior on FOS expression, brain ROIs (divided into left and right sides, where appropriate) were scanned by CellProfiler 4.2.1 to determine the total number of cells, as marked by DAPI. DAPI ROIs were shrunk to a point and then expanded by a factor of 6, and classified as being either FOS-positive or FOS-negative, as marked by presence of the secondary antibody (Alexa Fluor 555), using the same parameters for every slice. These per-ROI portions were then standardized using a Z-score between different histology days, to account for any batch effects of antibody binding or fluorescence. A linear regression model was used on a per-ROI basis, and a post-hoc tukey test was used to determine the effect of behavior on FOS expression, for each brain region. P-values were adjusted for multiple comparisions using the Holm method.

Relationship between PVN^{OT} calcium activity and behavior state, activity, and body temperature. To determine the effect of different behavioral states on calcium peak amplitude and frequency, we fit LMMs with amplitude or frequency as the dependent variable, behavioral state as the independent variable, and mouseID as a random effect. These models were run for both solo and paired conditions.

To determine the effect of social context and floor temperature on calcium peak amplitude and frequency, we fit LMMs with amplitude or frequency as the dependent variable, social context or floor temperature as the independent variable, and mouseID as a random effect.

To determine how calcium peak frequency is affected by behavioral state bout length (i.e., for quiescence and quiescent-huddle) and floor temperature, we fit a LMM with per-bout peak counts as the dependent variable; bout-length, floor temperature, and their interactions as the independent variables; and mouseID as the random effect. We subsequently extracted the standardized beta coefficients using the sjPlot package (Lüdecke, 2013).

To determine how locomotor activity changed during a 300 sec. interval of time surrounding calcium peaks (i.e., peri-peak time), we first z-scored the activity data (estimated at 10 Hz), then smoothed it according to the mean using the rollapply function (Zeileis et al., 2004), and finally calculated the per-second mean for each individual. Next, we calculated normalized activity data across the 600 sec interval, including the mean normalized activity before and after each peak (i.e., "before-after"). Last, we fit a LMM with normalized activity as the dependent variable, "before-after" as the independent variable, and mouse-ID as a random effect.

To determine peak probability during defined behaviors we used logistic regression. First, we used custom R code to (1) extract the onset and offset of behavioral bouts, and (2) label rows of data (at 10 frames per second) according to whether they occurred within a minute containing (or not containing) a calcium peak (i.e., PeakMinute). Next, we fit a binomial generalized linear model with PeakMinute as the dependent variable; the independent variable was the time span before, during, and after the behavioral epoch of interest (e.g., quiescence offset). Next, we extracted the per-frame predicted values (including standard error) from this model.

To compare the statistical distributions of Tb during calcium peaks *vs*. baseline, we plotted Tb according to the PeakMinute designation described above. We then used a LMM with Tb as the dependent variable; the independent variables were PeakMinute and mouseID as a random effect.

PVN^{OT} peak characteristics: before mating *vs.* early/late stages of lactation. To determine the effect of life-history phase (virgin, early-stage and late-stage lactation) on peak amplitude, FWHM, and interpeak interval we used LMMs with epoch (PPD 2-7; PPD 8-14; virgin) as a fixed effect and mouseID as a random effect to control for repeated measures. We performed posthoc tukey comparisons for each pairwise combination of fixed effect level using the emmeans package.

Effect of optogenetic stimulation on thermal profile. To determine the effect of light stimulation on Tb in ChR2+ and light-only controls separately, Tb data were binned per minute, with each value representing the mean of the 60 seconds following. We used a linear mixed-effects model (LMM) with Tb as the dependent variable, the interaction between light-status and minute as independent variables, and mouseID as a random effect. A post-hoc tukey test was used to determine per-minute differences.

To determine the effect of light stimulation on physical activity in ChR2+ vs. light-only controls separately, activity was binned per minute, and we used the same LMM as above, but with activity as the dependent variable.

To determine the effect of light stimulation on surface temperatures (BAT, rump, or dorsal surface) in ChR2+ vs. light-only controls separately, each surface temperature was analyzed separately, first by binning temps per minute, and then using the same LMM as above, with surface temps as the dependent variable.

To further determine the effect of light stimulation on direction of temperature change, slopes before and after light onset were analyzed with a second LMM that included fixed effects of time, proximity to stimulation (pre vs. post), and their interaction, plus a random intercept for mouse ID; frame-level weights were set to the inverse of each frame's temperature SD. A significant interaction term indicated that temperature trajectories differed between ChR2+ and control groups across the stimulation boundary.

To assess the effect of light stimulation on behavior in ChR2+ versus light-only controls, we quantified cumulative time spent in each behavioral state following stimulation. First, linear regression models were applied to individual arousal behaviors to evaluate their contribution to group differences. As no

single behavior showed a significant effect, all arousal behaviors were grouped, and a second linear regression model was used to assess whether total arousal time differed between groups.

References

Borchers HW. 2011. pracma: Practical Numerical Math Functions. doi:10.32614/CRAN.package.pracma

Landen JG, Vandendoren M, Killmer S, Bedford NL, Nelson AC. 2024. Huddling substates in mice facilitate dynamic changes in body temperature and are modulated by Shank3b and Trpm8 mutation. *Communications Biology* **7**:1186. doi:10.1038/s42003-024-06781-7

Liland KH, Mevik B-H. 2011. baseline: Baseline Correction of Spectra. doi:10.32614/CRAN.package.baseline

Lüdecke D. 2013. sjPlot: Data Visualization for Statistics in Social Science. doi:10.32614/CRAN.package.sjPlot

Tattersall G. 2019. gtatters/ThermImageJ: ThermImageJ. doi:10.5281/ZENODO.2652896

Van Boxtel G, Short T, Kienzle P. 2021. gsignal: Signal Processing. doi:10.32614/CRAN.package.gsignal

Wu Z, Xu Y, Zhu Y, Sutton AK, Zhao R, Lowell BB, Olson DP, Tong Q. 2012. An Obligate Role of Oxytocin Neurons in Diet Induced Energy Expenditure. *PLOS ONE* **7**:e45167. doi:10.1371/journal.pone.0045167

Zeileis A, Grothendieck G, Ryan JA. 2004. zoo: S3 Infrastructure for Regular and Irregular Time Series (Z's Ordered Observations). doi:10.32614/CRAN.package.zoo

Table S1

	Group	Model	Dep. Variable	Ind. Variable	Rndm effect	DF	T value	P-Val.
Fig. 1C								Adj:Holm
AHN	AH - QH	Linear Mod	%FOS(Zscore)	Behavior state	NA	78	5.09	2.96E-04
AHN	AH - SG	Linear Mod	%FOS(Zscore)	Behavior state		78	0.60	1.000
AHN	QH - SG	Linear Mod	%FOS(Zscore)	Behavior state		78	-3.30	0.146
ArcHN	AH - QH	Linear Mod	%FOS(Zscore)	Behavior state		50	3.29	0.173
ArcHN	AH - SG	Linear Mod	%FOS(Zscore)	Behavior state		50	2.92	0.422
ArcHN	QH - SG	Linear Mod	%FOS(Zscore)	Behavior state		50	-0.45	1.000
COLL	AH - QH	Linear Mod	%FOS(Zscore)	Behavior state		59	1.06	1.000
COLL	AH - SG	Linear Mod	%FOS(Zscore)	Behavior state		59	2.26	1.000
COLL	QH - SG	Linear Mod	%FOS(Zscore)	Behavior state		59	1.33	1.000
DmHN	AH - QH	Linear Mod	%FOS(Zscore)	Behavior state		64	5.80	2.80E-05
DmHN	AH - SG	Linear Mod	%FOS(Zscore)	Behavior state		64	4.43	4.22E-03
DmHN	QH - SG	Linear Mod	%FOS(Zscore)	Behavior state		64	-0.68	1.000
LH	AH - QH	Linear Mod	%FOS(Zscore)	Behavior state		150	12.72	0.00E+00
LH	AH - SG	Linear Mod	%FOS(Zscore)	Behavior state		150	2.73	0.568
LH	QH - SG	Linear Mod	%FOS(Zscore)	Behavior state		150	-7.94	6.62E-11
LPO	AH - QH	Linear Mod	%FOS(Zscore)	Behavior state		139	11.43	5.94E-13
LPO	AH - SG	Linear Mod	%FOS(Zscore)	Behavior state		139	3.28	0.136
LPO	QH - SG	Linear Mod	%FOS(Zscore)	Behavior state		139	-7.13	7.15E-09
LSR	AH - QH	Linear Mod	%FOS(Zscore)	Behavior state		105	11.28	1.68E-12
LSR	AH - SG	Linear Mod	%FOS(Zscore)	Behavior state		105	7.33	7.15E-09
LSR	QH - SG	Linear Mod	%FOS(Zscore)	Behavior state		105	-2.87	0.418
MamN	AH - QH	Linear Mod	%FOS(Zscore)	Behavior state		125	6.91	2.99E-08
MamN	AH - SG	Linear Mod	%FOS(Zscore)	Behavior state		125	2.18	1.000
MamN	QH - SG	Linear Mod	%FOS(Zscore)	Behavior state		125	-4.32	3.62E-03
MePO	AH - QH	Linear Mod	%FOS(Zscore)	Behavior state		46	2.39	1.000
MePO	AH - SG	Linear Mod	%FOS(Zscore)	Behavior state		46	0.43	1.000
MePO	QH - SG	Linear Mod	%FOS(Zscore)	Behavior state		46	-1.80	1.000
MPO	AH - QH	Linear Mod	%FOS(Zscore)	Behavior state		53	2.46	1.000
MPO	AH - SG	Linear Mod	%FOS(Zscore)	Behavior state		53	0.52	1.000
MPO	QH - SG	Linear Mod	%FOS(Zscore)	Behavior state		53	-1.67	1.000
PAG	AH - QH	Linear Mod	%FOS(Zscore)	Behavior state		101	10.15	1.86E-12
PAG	AH - SG	Linear Mod	%FOS(Zscore)	Behavior state		101	-0.18	1.000
PAG	QH - SG	Linear Mod	%FOS(Zscore)	Behavior state		101	-9.64	2.03E-12
PH	AH - QH	Linear Mod	%FOS(Zscore)	Behavior state		99	10.96	1.03E-08
PH	AH - SG	Linear Mod	%FOS(Zscore)	Behavior state		99	3.07	0.249
PH	QH - SG	Linear Mod	%FOS(Zscore)	Behavior state		99	-6.79	1.20E-07
PVN	AH - QH	Linear Mod	%FOS(Zscore)	Behavior state		101	5.42	5.21E-05
PVN	AH - SG	Linear Mod	%FOS(Zscore)	Behavior state		101	4.52	2.02E-03
PVN	QH - SG	Linear Mod	%FOS(Zscore)	Behavior state		101	-0.08	1.000
SCN	AH - QH	Linear Mod	%FOS(Zscore)	Behavior state		78	2.41	1.000
SCN	AH - SG	Linear Mod	%FOS(Zscore)	Behavior state		78	0.94	1.000
SCN	QH - SG	Linear Mod	%FOS(Zscore)	Behavior state		78	-1.02	1.000
SON	AH - QH	Linear Mod	%FOS(Zscore)	Behavior state		56	2.33	1.000
SON	AH - SG	Linear Mod	%FOS(Zscore)	Behavior state		56	1.51	1.000
SON	QH - SG	Linear Mod	%FOS(Zscore)	Behavior state		56	-0.50	1.000
SubTN	AH - QH	Linear Mod	%FOS(Zscore)	Behavior state		60	3.17	0.222
SubTN	AH - SG	Linear Mod	%FOS(Zscore)	Behavior state		60	0.72	1.000
SubTN	QH - SG	Linear Mod	%FOS(Zscore)	Behavior state		60	-1.72	1.000

TubN	AH - QH	Linear Mod	%FOS(Zscore)	Behavior state		55	2.69	0.705
TubN	AH - SG	Linear Mod	%FOS(Zscore)	Behavior state		55	2.62	0.818
TubN	QH - SG	Linear Mod	%FOS(Zscore)	Behavior state		55	-0.31	1.000
VmHN	AH - QH	Linear Mod	%FOS(Zscore)	Behavior state		57	4.07	1.60E-02
VmHN	AH - SG	Linear Mod	%FOS(Zscore)	Behavior state		57	1.69	1.000
VmHN	QH - SG	Linear Mod	%FOS(Zscore)	Behavior state		57	-2.06	1.000
Figure 1I								
PVNOT	dorAH - venAH	lmer/Tukey	% *Fos*	Region*behavior	mouseID	27.54	4.31	1.01E-03
	dorAH - dorQH	lmer/Tukey	% *Fos*	Region*behavior	mouseID	8.74	3.30	3.94E-02
	dorAH - venQH	lmer/Tukey	% *Fos*	Region*behavior	mouseID	8.74	1.81	0.333
	venAH - dorQH	lmer/Tukey	% *Fos*	Region*behavior	mouseID	8.59	0.23	0.996
	venAH - venQH	lmer/Tukey	% *Fos*	Region*behavior	mouseID	8.59	-1.30	0.587
	dorQH - venQH	lmer/Tukey	% *Fos*	Region*behavior	mouseID	27.17	-1.52	0.438

	Group	Model	Dep. Variable	Ind. Variable	Rndm effect	DF	T value	P-Val.
Fig. 2F								
Solo	EatDrink	lmer	Amplitude	Behavior	mouseID	34.75831	0.07498	0.941
	Groom	lmer	Amplitude	Behavior	mouseID	34.75831	0.26705	0.791
	LMA	lmer	Amplitude	Behavior	mouseID	34.75831	0.32409	0.748
	Nest	lmer	Amplitude	Behavior	mouseID	34.75831	2.83207	7.64E-03
	Quiescent	lmer	Amplitude	Behavior	mouseID	34.75831	8.85183	1.98E-10
	Stationary	lmer	Amplitude	Behavior	mouseID	34.77749	0.11229	0.911
Fig. 2G								
Solo	EatDrink	lmer	Frequency	Behavior	mouseID	34.62	0.09650	0.924
	Groom	lmer	Frequency	Behavior	mouseID	34.62	0.32166	0.750
	LMA	lmer	Frequency	Behavior	mouseID	34.62	0.32166	0.750
	Nest	lmer	Frequency	Behavior	mouseID	34.62	3.17483	3.14E-03
	Quiescent	lmer	Frequency	Behavior	mouseID	34.62	9.45694	4.00E-11
	Stationary	lmer	Frequency	Behavior	mouseID	34.68	0.13502	0.893
Fig. 2I								
Paired	Active huddle	lmer	Amplitude	Behavior	mouseID	56	5.25932	2.35E-06
	Contact_Init	lmer	Amplitude	Behavior	mouseID	56	0	1.000
	Contact_Rec	lmer	Amplitude	Behavior	mouseID	56	0.06867	0.945
	EatDrink	lmer	Amplitude	Behavior	mouseID	56	0.72183	0.473
	Groom	lmer	Amplitude	Behavior	mouseID	56	0	1.000
	LMA	lmer	Amplitude	Behavior	mouseID	56	0.19394	0.847
	NA	lmer	Amplitude	Behavior	mouseID	56	0	1.000
	Nest	lmer	Amplitude	Behavior	mouseID	56	1.83891	0.071
	Quiscent huddle	lmer	Amplitude	Behavior	mouseID	56	16.74134	1.84E-23
	Quiescent	lmer	Amplitude	Behavior	mouseID	56	1.88315	0.065
	Stationary	lmer	Amplitude	Behavior	mouseID	56	0	1.000
Fig. 2J								
Paired	Active huddle	lmer	Amplitude	Behavior	mouseID	56	5.25932	2.35E-06
	Contact_Init	lmer	Amplitude	Behavior	mouseID	56	0	1.000
	Contact_Rec	lmer	Amplitude	Behavior	mouseID	56	0.06867	0.945
	EatDrink	lmer	Amplitude	Behavior	mouseID	56	0.72183	0.473
	Groom	lmer	Amplitude	Behavior	mouseID	56	0	1.000
	LMA	lmer	Amplitude	Behavior	mouseID	56	0.19394	0.847
	NA	lmer	Amplitude	Behavior	mouseID	56	0	1.000
	Nest	lmer	Amplitude	Behavior	mouseID	56	1.83891	0.071
	Quiscent huddle	lmer	Amplitude	Behavior	mouseID	56	16.74134	1.84E-23

	Quiescent	lmer	Amplitude	Behavior	mouseID	56	1.88315	0.065
	Stationary	lmer	Amplitude	Behavior	mouseID	56	0	1.000
Fig. 2K							statistic	
Solo:Quies.	Ta_15 - Ta_23	lmer/Tukey	Frequency	AmbientTemp	mouseID	16.11576	-0.23860	0.969
	Ta_15 - Ta_29	lmer/Tukey	Frequency	AmbientTemp	mouseID	17.07043	-3.35101	0.010
	Ta_23 - Ta_29	lmer/Tukey	Frequency	AmbientTemp	mouseID	17.07517	-3.22980	0.013
Fig. 2N								
Paired:QH	Ta_15 - Ta_23	lmer/Tukey	Frequency	AmbientTemp	mouseID	15.27282	-1.85294	0.186
	Ta_15 - Ta_29	lmer/Tukey	Frequency	AmbientTemp	mouseID	15.60255	-1.64613	0.257
	Ta_23 - Ta_29	lmer/Tukey	Frequency	AmbientTemp	mouseID	15.53927	0.14852	0.988

	Group	Model	Dep. Variable	Ind. Variable	Rndm effect	DF	T value	P-Val.
Fig. 3C								
PeriCa2+peak	Solo	lmer	PhysicalActiv.	after vs before	MouseID	7.00	3.37	0.012
Fig. 3E								
PeriCa2+peak	Paired	lmer	PhysicalActiv.	after vs before	MouseID	6.00	6.62	0.001
Fig. 3K								
Nesting	Pre-quies.	lmer	PeakFreq	Quiesence phase	MouseID	32.26	1.71	0.097
	Post-quies.	lmer	PeakFreq	Quiesence phase	MouseID	35.28	2.97	0.005
	Pre and Post	lmer	PeakFreq	Quiesence phase	MouseID	20.54	1.96	0.064
	Neither	lmer	PeakFreq	Quiesence phase	MouseID	10.47	2.37	0.038
Fig. 3M								
Act.Huddle	Pre-quies.	lmer	PeakFreq	Quiesence phase	MouseID	65.44	0.60	0.548
	Post-quies.	lmer	PeakFreq	Quiesence phase	MouseID	50.88	4.08	0.000
	Pre and Post	lmer	PeakFreq	Quiesence phase	MouseID	26.61	1.58	0.127
	Neither	lmer	PeakFreq	Quiesence phase	MouseID	21.42	4.42	0.000
Fig. 3N								
Solo Tb	Peak: binary	lmer	BodyTemp	PeakType	MouseID	968662.28	-38.85	0.000
Fig. 3P								
Paired Tb	Peak: binary	lmer	BodyTemp	PeakType	MouseID	764606.10	-42.78	0.000

	Group	Model	Dep. Variable	Ind. Variable	Rndm effect	DF	T value	P-Val.
Fig. 4I								
FWHM	lac_2_7 - lac_8_14	lmer	FWHM	Lactation phase	MouseID	170.07	0.63	0.806
	lac_2_7 - virgin	lmer	FWHM	Lactation phase	MouseID	170.54	3.51	1.68E-03
	lac_8_14 - virgin	lmer	FWHM	Lactation phase	MouseID	170.40	3.31	3.27E-03
Fig. 4J								
Amplitude	lac_2_7 - lac_8_14	lmer	PeakAmplitud	Lactation phase	MouseID	170.06	-5.56	4.75E-06
	lac_2_7 - virgin	lmer	PeakAmplitud	Lactation phase	MouseID	170.49	1.15	0.485
	lac_8_14 - virgin	lmer	PeakAmplitud	Lactation phase	MouseID	170.36	4.97	4.75E-06
Fig. 4K								
IPI	lac_2_7 - lac_8_14	lmer	IntrPeakIntrvl	Lactation phase	MouseID	167.90	1.24	0.431
	lac_2_7 - virgin	lmer	IntrPeakIntrvl	Lactation phase	MouseID	104.73	-1.95	0.130
	lac_8_14 - virgin	lmer	IntrPeakIntrvl	Lactation phase	MouseID	135.08	-2.92	1.15E-02

	Group	Model	Dep. Variable	Ind. Variable	Rndm effect	DF	T value	P-Val.
Fig. 5G								
Slope	Dorsal surface	lmer	Surface temp	Time* Event	MouseID	2793	7.85	5.89E-15
Fig. 5H								
Mean	Dorsal surface	lmer	Surface temp	Peri event	MouseID	2793	2.48	0.0133
Fig. 5I								

Slope	BAT surface	lmer	Surface temp	Time* Event	MouseID	2793	18.08	3.00E-69
Fig. 5J								
Mean	BAT surface	lmer	Surface temp	Peri event	MouseID	2793	2.72	0.0065
Fig. 5K								
Slope	Rump surface	lmer	Surface temp	Time* Event	MouseID	2620	0.03	0.976
Fig. 5L								
Mean	Rump surface	lmer	Surface temp	Peri event	MouseID	2620	3.13	0.0018

	Group	Model	Dep. Variable	Ind. Variable	Rndm effect	DF	T value	P-Val.
Fig. 6C								
Low Tb-T0	0 sec	lmer	Core Tb	Binned time	MouseID	Inf	-0.779	0.436
	60 sec	lmer	Core Tb	Binned time	MouseID	Inf	-0.577	0.564
	120 sec	lmer	Core Tb	Binned time	MouseID	Inf	-0.515	0.606
	180 sec	lmer	Core Tb	Binned time	MouseID	Inf	-0.097	0.923
	240 sec	lmer	Core Tb	Binned time	MouseID	Inf	-0.029	0.977
	300 sec	lmer	Core Tb	Binned time	MouseID	Inf	0.554	0.580
	360 sec	lmer	Core Tb	Binned time	MouseID	Inf	1.524	0.128
	420 sec	lmer	Core Tb	Binned time	MouseID	Inf	2.235	0.025
	480 sec	lmer	Core Tb	Binned time	MouseID	Inf	2.133	0.033
	540 sec	lmer	Core Tb	Binned time	MouseID	Inf	1.971	0.049
Fig. 6D								
Low Tb-T0	0 sec	lmer	Physical activity	Binned time	MouseID	4.45	0.452	0.673
	60 sec	lmer	Physical activity	Binned time	MouseID	4.62	0.402	0.705
	120 sec	lmer	Physical activity	Binned time	MouseID	4.66	0.627	0.560
	180 sec	lmer	Physical activity	Binned time	MouseID	4.72	0.325	0.759
	240 sec	lmer	Physical activity	Binned time	MouseID	4.80	0.833	0.444
	300 sec	lmer	Physical activity	Binned time	MouseID	5.01	0.763	0.480
	360 sec	lmer	Physical activity	Binned time	MouseID	5.22	0.774	0.472
	420 sec	lmer	Physical activity	Binned time	MouseID	5.38	1.734	0.139
	480 sec	lmer	Physical activity	Binned time	MouseID	5.48	1.389	0.219
	540 sec	lmer	Physical activity	Binned time	MouseID	6.14	1.673	0.144
Fig. 6E								
Low Tb-T0	0 sec	lmer	BAT temp	Binned time	MouseID	Inf	-0.414	0.6787
	60 sec	lmer	BAT temp	Binned time	MouseID	Inf	-2.218	0.0265
	120 sec	lmer	BAT temp	Binned time	MouseID	Inf	-2.765	0.0057
	180 sec	lmer	BAT temp	Binned time	MouseID	Inf	-0.315	0.7528
	240 sec	lmer	BAT temp	Binned time	MouseID	Inf	-0.427	0.6696
	300 sec	lmer	BAT temp	Binned time	MouseID	Inf	0.934	0.3504
	360 sec	lmer	BAT temp	Binned time	MouseID	Inf	3.427	6.09E-04
	420 sec	lmer	BAT temp	Binned time	MouseID	Inf	5.866	4.46E-09
	480 sec	lmer	BAT temp	Binned time	MouseID	Inf	8.111	5.04E-16
	540 sec	lmer	BAT temp	Binned time	MouseID	Inf	10.508	7.94E-26
Fig. 6F								
Low Tb-T0	0 sec	lmer	Rump temp	Binned time	MouseID	Inf	0.096	0.9236
	60 sec	lmer	Rump temp	Binned time	MouseID	Inf	1.495	0.1350
	120 sec	lmer	Rump temp	Binned time	MouseID	Inf	2.388	0.0169
	180 sec	lmer	Rump temp	Binned time	MouseID	Inf	2.207	0.0273
	240 sec	lmer	Rump temp	Binned time	MouseID	Inf	3.056	2.24E-03
	300 sec	lmer	Rump temp	Binned time	MouseID	Inf	4.717	2.39E-06
	360 sec	lmer	Rump temp	Binned time	MouseID	Inf	6.921	4.48E-12
	420 sec	lmer	Rump temp	Binned time	MouseID	Inf	10.140	3.66E-24

	480 sec	lmer	Rump temp	Binned time	MouseID	Inf	12.047	2.00E-33
	540 sec	lmer	Rump temp	Binned time	MouseID	Inf	12.132	7.16E-34

	Group	Model	Dep. Variable	Ind. Variable	Rndm effect	DF	T value	P-Val.
Fig. S2C								
	Paired vs. solo	lmer	Amplitude	Social context	mouseID	6.842	1.540	0.168
Fig. S2D								
	Paired vs. solo	lmer	Peak freq.	Social context	mouseID	43.298	2.455	1.82E-02
Fig. S2G								
Solo	EatDrink	lmer	Amplitude	Behavior	mouseID	57.583	-0.615	0.541
	Groom	lmer	Amplitude	Behavior	mouseID	56.462	-0.430	0.669
	LMA	lmer	Amplitude	Behavior	mouseID	56.462	-0.390	0.698
	Nest	lmer	Amplitude	Behavior	mouseID	53.692	2.346	2.27E-02
	Quiescent	lmer	Amplitude	Behavior	mouseID	53.692	8.041	8.81E-11
	Stationary	lmer	Amplitude	Behavior	mouseID	98.181	0.296	0.768
Fig. S2I								
Solo	EatDrink	lmer	Frequency	Behavior	mouseID	39.71	0.08	0.939
	Groom	lmer	Frequency	Behavior	mouseID	37.58	0.34	0.734
	LMA	lmer	Frequency	Behavior	mouseID	37.58	0.30	0.765
	Nest	lmer	Frequency	Behavior	mouseID	35.65	3.94	3.68E-04
	Quiescent	lmer	Frequency	Behavior	mouseID	35.65	10.51	1.83E-12
	Stationary	lmer	Frequency	Behavior	mouseID	100.21	0.31	0.758
Fig. S2H								
Paired	Active huddle	lmer	Amplitude	Behavior	mouseID	160	3.4057	8.34E-04
	Contact_Init	lmer	Amplitude	Behavior	mouseID	160	-0.6678	0.505
	Contact_Rec	lmer	Amplitude	Behavior	mouseID	160	-0.5620	0.575
	EatDrink	lmer	Amplitude	Behavior	mouseID	160	-0.1131	0.910
	Groom	lmer	Amplitude	Behavior	mouseID	160	-0.5501	0.583
	LMA	lmer	Amplitude	Behavior	mouseID	160	-0.5109	0.610
	NA	lmer	Amplitude	Behavior	mouseID	160	-0.0953	0.924
	Nest	lmer	Amplitude	Behavior	mouseID	160	1.0442	0.298
	Quiscent huddle	lmer	Amplitude	Behavior	mouseID	160	14.1307	6.05E-30
	Quiescent	lmer	Amplitude	Behavior	mouseID	160	0.8782	0.381
	Stationary	lmer	Amplitude	Behavior	mouseID	160	-0.3739	0.709
Fig. S2J								
Paired	Active huddle	lmer	Frequency	Behavior	mouseID	123.7290	6.1241	1.12E-08
	Contact_Init	lmer	Frequency	Behavior	mouseID	126.9801	-0.0020	0.998
	Contact_Rec	lmer	Frequency	Behavior	mouseID	126.9676	0.1419	0.887
	EatDrink	lmer	Frequency	Behavior	mouseID	126.9801	0.9498	0.344
	Groom	lmer	Frequency	Behavior	mouseID	134.2063	0.0007	0.999
	LMA	lmer	Frequency	Behavior	mouseID	126.9801	0.2926	0.770
	NA	lmer	Frequency	Behavior	mouseID	161.9678	0.0370	0.971
	Nest	lmer	Frequency	Behavior	mouseID	126.9676	2.5441	1.22E-02
	Quiscent huddle	lmer	Frequency	Behavior	mouseID	123.7290	16.1268	3.33E-32
	Quiescent	lmer	Frequency	Behavior	mouseID	131.7690	1.8253	0.070
	Stationary	lmer	Frequency	Behavior	mouseID	159.3348	-0.0252	0.980

	Group	Model	Dep. Variable	Ind. Variable	Rndm effect	DF	T value	P-Val.
Fig. S3I								
	Quiesence	lmer	NearZero dF/F	offsetVS.onset	mouseID	7	5.035	1.51E-03
Fig. S3J								

	Quies. Huddle	lmer	NearZero dF/F	offsetVS.onset	mouseID	6	3.299	1.64E-02
Fig. S3K							statistic	
Nesting	pre - post	lmer	Sum of bouts	Rest_Phase	mouseID	135.0469	3.708	1.71E-03
	pre - both	lmer	Sum of bouts	Rest_Phase	mouseID	135.0206	2.422	0.078
	pre - neither	lmer	Sum of bouts	Rest_Phase	mouseID	135.0780	-5.177	4.75E-06
	post - both	lmer	Sum of bouts	Rest_Phase	mouseID	135.0742	-1.234	0.606
	post - neither	lmer	Sum of bouts	Rest_Phase	mouseID	135.0514	-8.989	1.60E-14
	both - neither	lmer	Sum of bouts	Rest_Phase	mouseID	135.1052	-7.565	3.22E-11
Fig. S2L							statistic	
ActiveHudd	pre - post	lmer	Sum of bouts	Rest_Phase	mouseID	68.08	3.71	2.31E-03
	pre - both	lmer	Sum of bouts	Rest_Phase	mouseID	68.08	3.46	5.10E-03
	pre - neither	lmer	Sum of bouts	Rest_Phase	mouseID	68.01	-2.03	0.19
	post - both	lmer	Sum of bouts	Rest_Phase	mouseID	68.19	-0.25	0.995
	post - neither	lmer	Sum of bouts	Rest_Phase	mouseID	68.08	-5.72	1.56E-06
	both - neither	lmer	Sum of bouts	Rest_Phase	mouseID	68.08	-5.46	4.21E-06

	Group	Model	Dep. Variable	Ind. Variable	Rndm effect	DF	T value	P-Val.
Fig. S4B								
ChR2	Arousal	lmer	Cum. Time	Group	MouseID	152	1.8928	0.0603
	Quiescence	lmer	Cum. Time	Group	MouseID	152	-0.3042	0.7614
Fig. S4C								
ChR2	Low Tb-T0	lmer	Physical activity	Time * Group	MouseID	705	-2.0477	4.10E-02
	High Tb-T0	lmer	Physical activity	Time * Group	MouseID	616	1.9036	0.0574
Fig. S4D								
ChR2	Low Tb-T0	lmer	BAT temp	Time * Group	MouseID	595	-3.1796	1.55E-03
	High Tb-T0	lmer	BAT temp	Time * Group	MouseID	521	1.8330	0.0674
Fig. S4E								
ChR2	Low Tb-T0	lmer	Rump temp	Time * Group	MouseID	588	-5.7331	1.58E-08
	High Tb-T0	lmer	Rump temp	Time * Group	MouseID	520	1.2131	0.2256
Fig. S4F								
ChR2	Low Tb-T0	lmer	Dorsal temp	Time * Group	MouseID	588	-4.7657	2.37E-06
	High Tb-T0	lmer	Dorsal temp	Time * Group	MouseID	519	2.4031	1.66E-02

Supplementary Figures

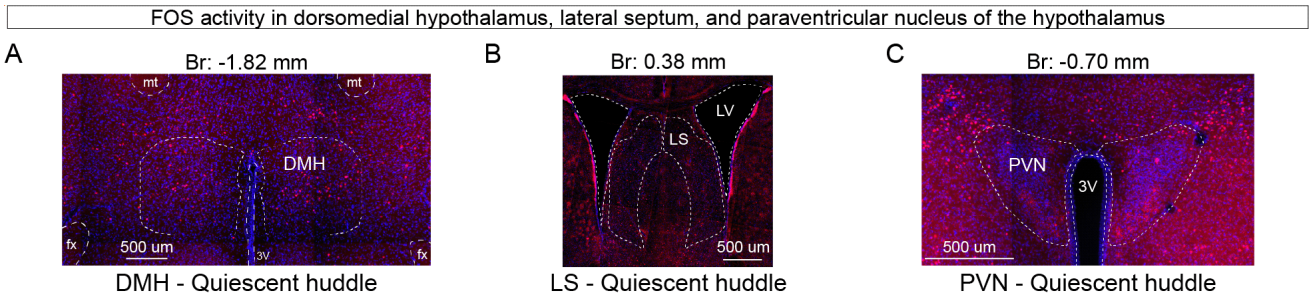

Figure S1. Histology of FOS activity in the DMH, LS, and PVN. Related to Figure 1.
(A - C) Representative histology images showing quiescent huddling associated FOS expression in the DMH (A), LS (B), and PVN (C). 3V: third ventricle; mt: mammillothalamic tract.

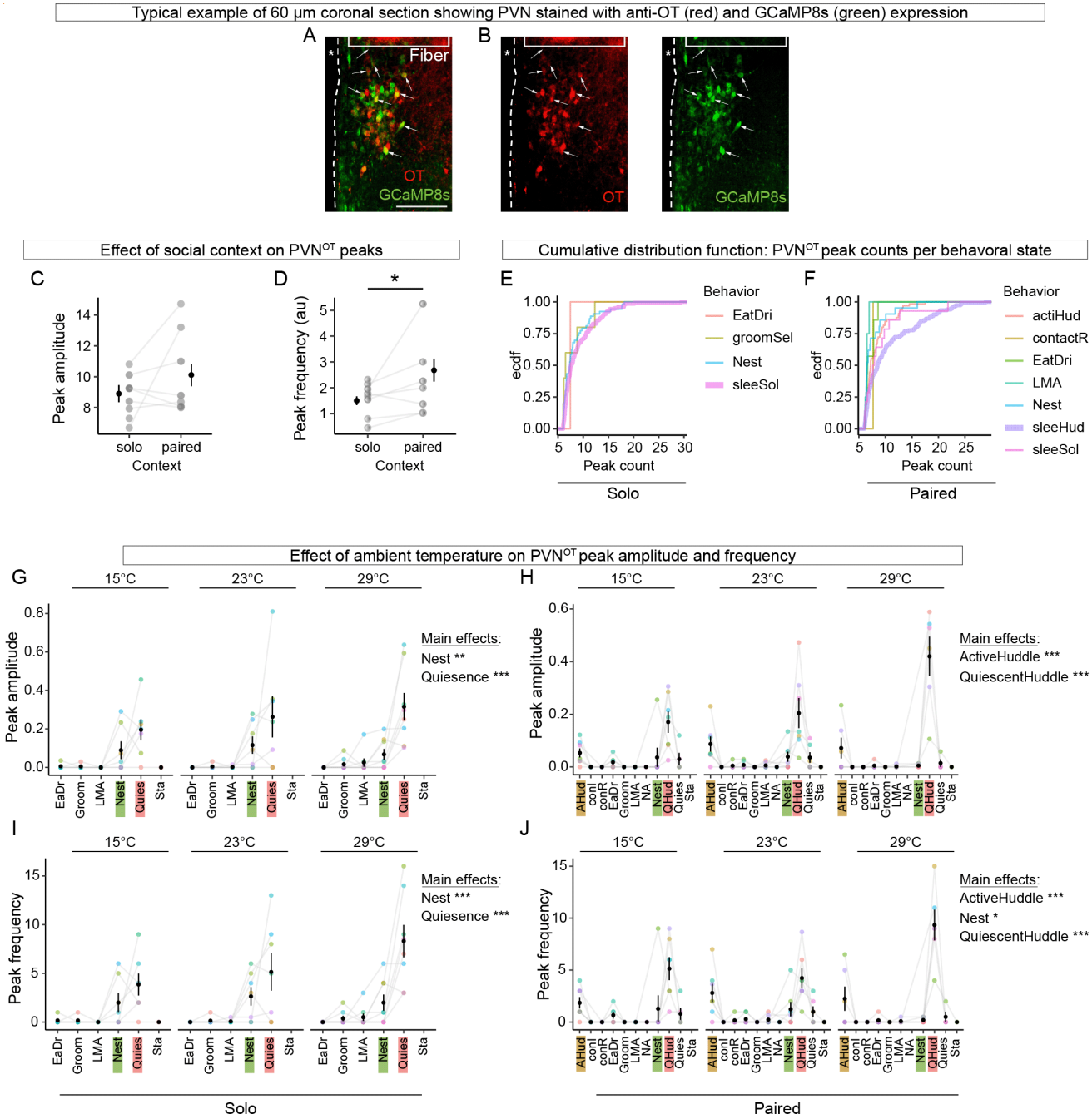

Figure S2. Characterization of PVN^{OT} Ca^{2+} peaks and their associations with behavioral states. Related to Figure 2.
(A - B) Representative coronal brain slice showing the location of the optical fiber and expression of oxytocin peptide (red) and GCaMP8s (green) in the PVN. Arrows indicate some cells co-labeled with GCaMP8s and anti-OT. The third ventricle is designated by "*". Scale bar 100 µm.
(C - D) Effect of social context on PVN^{OT} peak amplitude **(C)** and frequency **(D)**.
(E - F) PVN^{OT} empirical cumulative distribution functions (ecdf) of peak counts according to behavioral state in solo **(E)** and paired **(F)** conditions.
(G - H) Effect of floor temperature on PVN^{OT} peak amplitude. Relationship between floor temperature and behavior state in solo **(F)** and paired **(G)** females.
(I - J) Effect of floor temperature on PVN^{OT} peak frequency. Relationship between floor temperature and behavior state in solo **(I)** and paired **(J)** females.
Statistical results are from linear mixed models. N = 8 solo, N = 7 paired, N = 50 recordings. Data shows mean ±SEM. $P < 0.05$ *, $P < 0.01$ **, $P < 0.001$ ***.

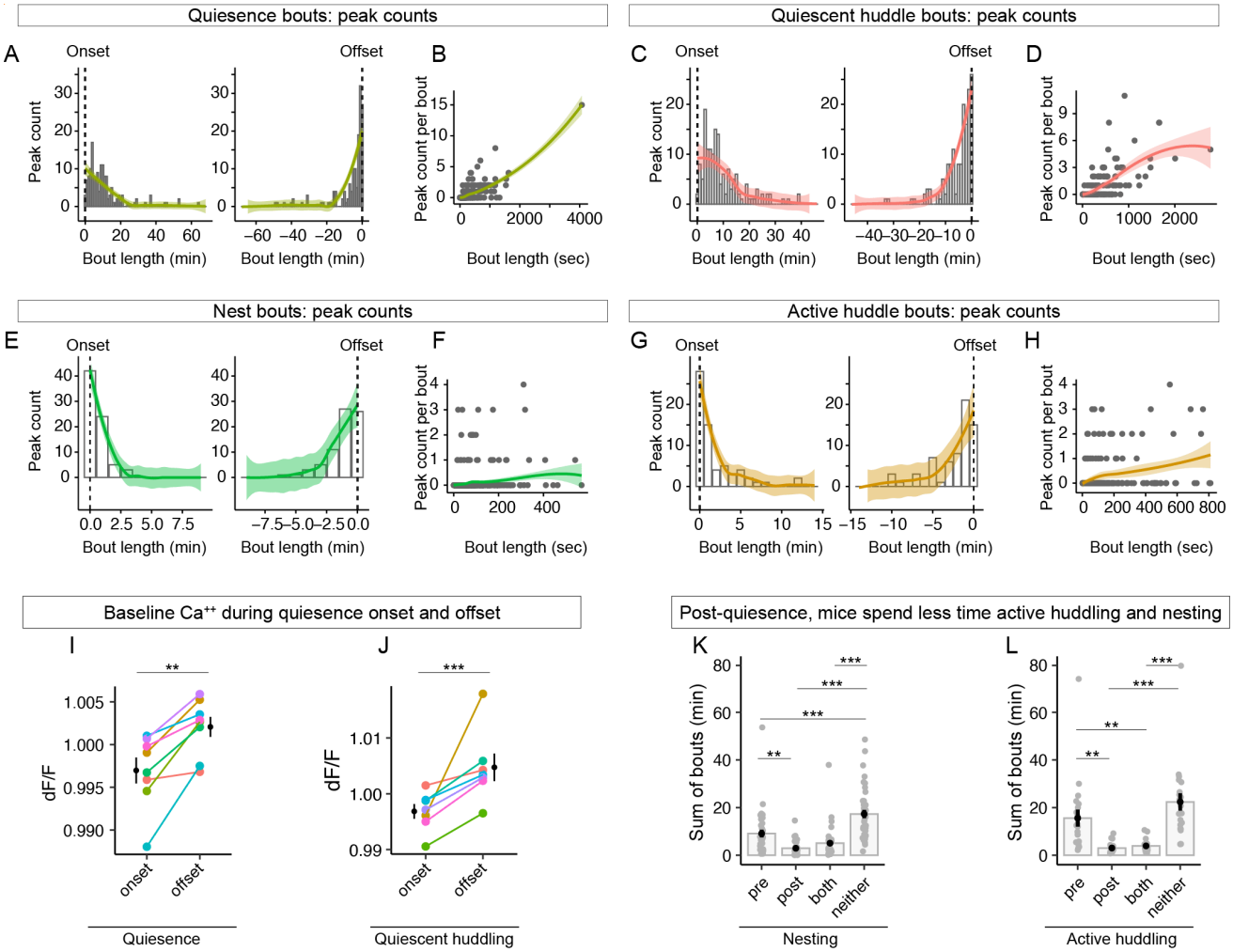

Figure S3. PVN^{OT} Ca^{2+} peaks during behavioral states and transitions. Related to Figure 3.
(A - D) Peak counts for bouts of resting behaviors. Quiescence onset/offset peak counts **(A)** and peak count per bout **(B)**. Quiescence huddle onset/offset peaks counts **(C)** and relationship between bout length and peak count **(D)**.
(E - H) Peaks counts for bouts of active behaviors. Nesting onset/offset peaks counts **(E)** and relationship between bout length and peak count **(F)**. Active huddle onset/offset peak counts **(G)** and relationship between bout length and peak count **(H)**.
(I - J) Per-individual means of Ca^{++} dF/F during onset and offset (i.e., near-zero values) of two resting behaviors: quiescence **(I)** and quiescent huddle **(J)**.
(K - L) Sum of bouts according to the phase of quiescence. “Neither” refers to bouts that did not adjoin bouts of quiescence. Nesting bouts **(K)**. Active huddling bouts **(L)**. Post quiescence nesting and active huddling is relatively rare. **I-L**: linear mixed model. **F,H,J,L**: logistic regression. N = 8 mice/50 recordings; all data shows mean ±SEM. $P < 0.05$ *, $P < 0.01$ **, $P < 0.001$ ***. Full statistical analysis in Table S1.

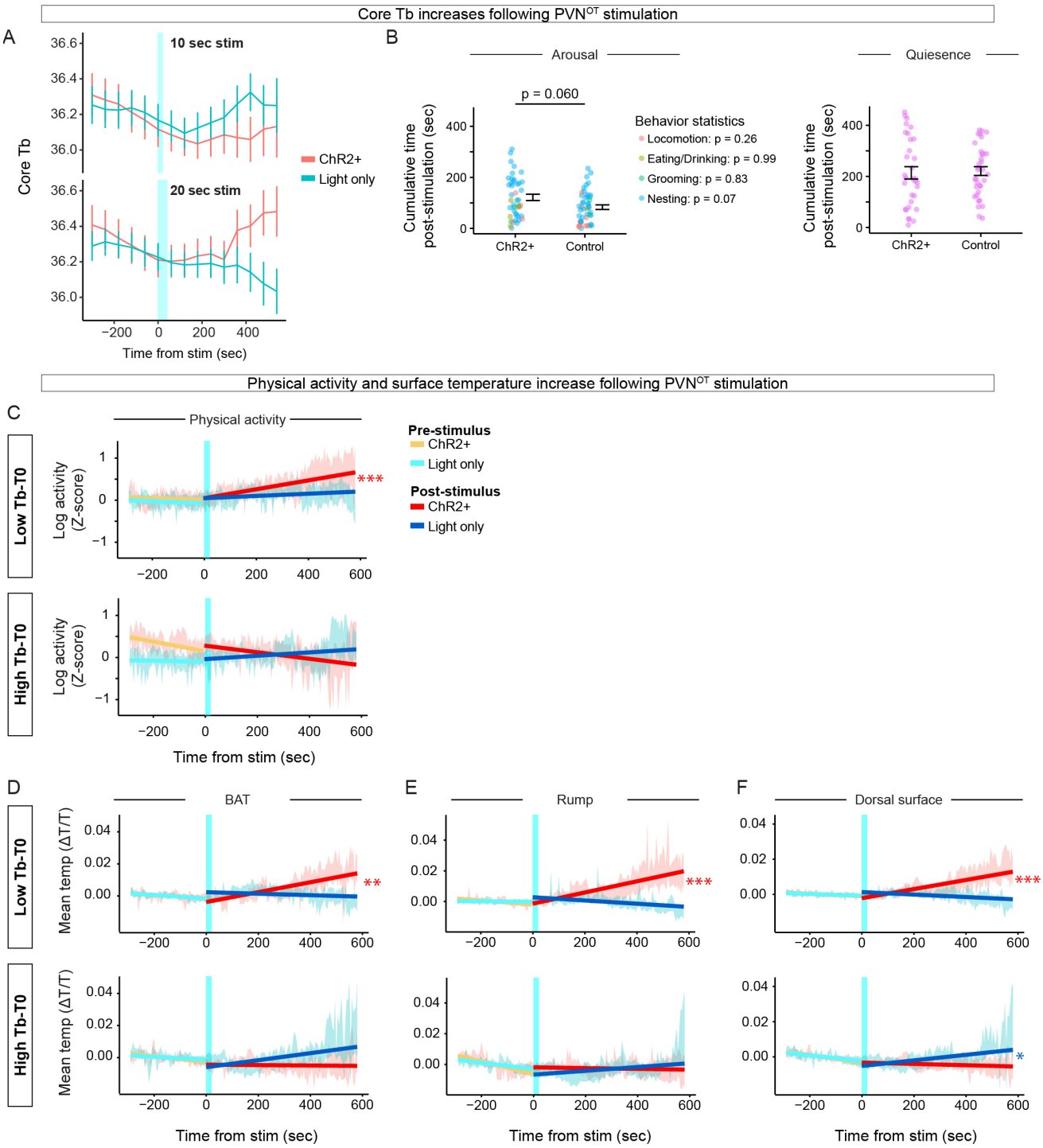

Figure S4. During low-Tb rest state, optogenetic stimulation of PVN^{OT} neurons increases and physical activity and thermogenesis. Related to Figure 6.

(A) Blue light stimulation (time 0; shaded blue rectangle) during 20s vs. 10s stimulations in ChR2+ animals compared to light-only animals.

(B) Cumulative time spent in arousal/awake (left) and rest/quiescent (right) behaviors following 20s PVN^{OT} stimulation. Each point represents a trial, color-coded by behavior. Black bars show mean ± SEM.

(C) Linear regressio line ± SEM of physical activity (log-transformed Z-score) 5 min before and 10 min following 20s PVN^{OT} stimulation.

(D - F) Same analysis as in **(C)** for surface temperatures (ΔT/T) of BAT **(D)**, rump **(E)**, and dorsal surface **(F)**. Stimulation in ChR2+ animals significantly increased temperatures in the low Tb-T0 group, with opposite or no effect in the high Tb-T_0 group. P < 0.05 *, P < 0.01 **, P < 0.001 ***. Full statistical analysis in Table S1.

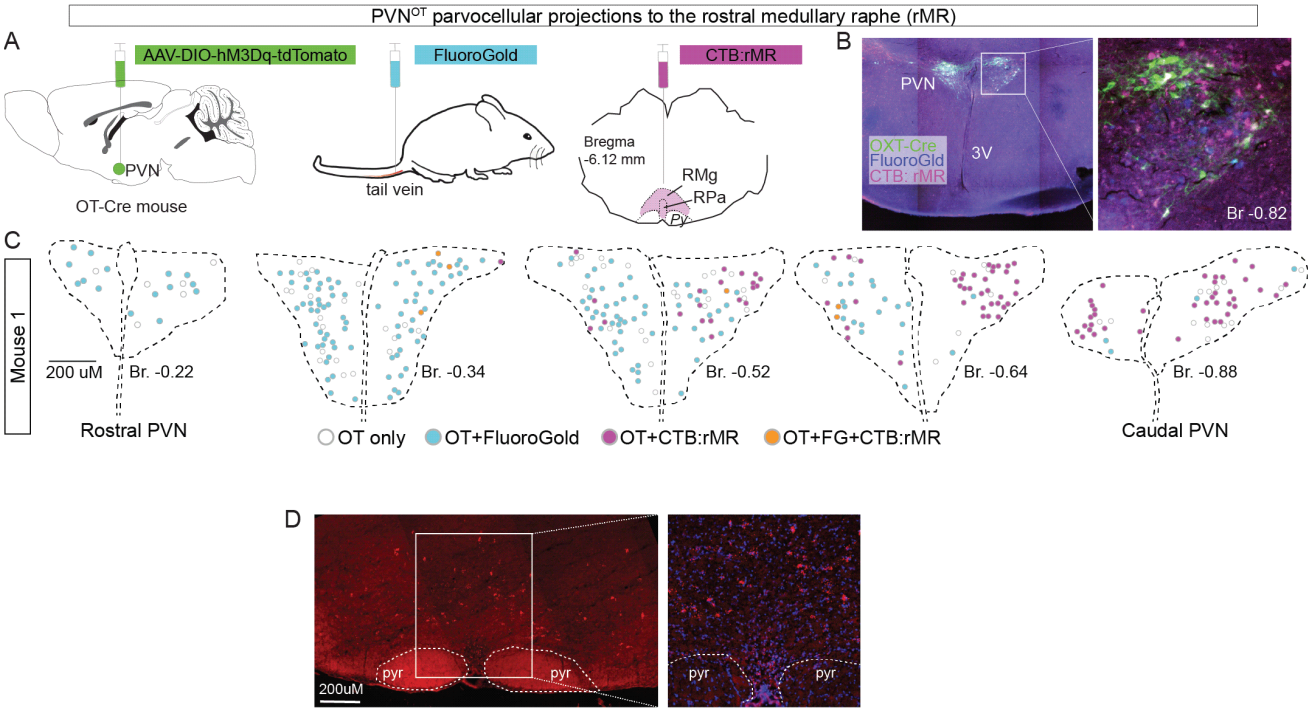

Figure S5. PVN^{OT} parvocellular projections to the rostral medullary raphe.
(A-D) PVN^{OT} parvocellular projections to the rostral medullary raphe (rMR). Scheme of injections to label magno- and parvocellular OT neurons **(A)**. Representative histology showing cells labeled for OXT-Cre, FluoroGold, and CTB **(B)**. Distribution of PVN^{OT} neurons retrogradely labeled with FluoroGold and CTB **(C)**. Each map was made from one coronal section. Cells double-labeled with FluoroGold and OT-Cre were mostly distributed in the rostral part of the PVN; cells double-labeled with CTB and OT-Cre were in the caudal part of the PVN **(C)**. Fluorescent in situ hybridization of OXTR (red) in the rMR region **(D)**.

Video Legends

Video S1. Photometry recording of virgin mouse in the homecage. A large-amplitude PVN^{OT} peak occurs at 0:00:03s. Video is sped up to 4x.

VideoS2. Photometry recording of a dam in the homecage with pups on PPD 14. The first large-amplitude PVN^{OT} peaks occur at approximately 0:00:07s. Even larger peaks, typical of late-stage lactation occur at 0:00:19s and 0:01:16s . Video is sped up to 4x.

VideoS3. SGBS enables real-time segmentation of thermally defined anatomical features in freely moving mice. Example video shows the output of the SGBS model, which accurately identifies and tracks three anatomical regions – BAT, rump, and dorsal surface – in a freely moving mouse in the homecage using thermal imaging. Video is sped up to 4x.

Key Resources Table

Reagent type	Designation	Source or reference	Identifiers	Additional information
chemical compound	DAPI mounting medium	Vectashield	H-2000	
chemical compound	NGS	Jackson ImmunoResearch	005-000-121	10%
chemical compound	Prolong Gold mounting medium	Invitrogen	P36930	
chemical compound	Far-red (640) Nissl stain	Thermofisher Scientific	N21483	(1:80)
chemical compound	Fluoro-Gold	Fluorochrome		
chemical compound	Capsaicin	EMD Millipore	211275	0.25 mg/mL
antibody	c-Fos (9F6), rabbit mAb	Cell Signaling	14609	(1:1000)
antibody	Alexa Fluor Plus 555, goat, anti-rabbit IgG	Thermo Scientific	A32732	(1:500)
strain	Oxytocin-Ires-Cre	Jackson Laboratory	024234	Bred/maintained at UW
strain	C57B6/J	Jackson Laboratory	000664	Bred/maintained at UW
recombinant DNA	pGP-AAV9-syn-FLEX-jGCaMP8s-WPRE	Addgene	162377	2.7 x 10^13 gc/mL
recombinant DNA	AAVDJ-EF1a-DIO-hChR2(H134R)-EYFP-WPRE-pA	Salk		4.03 x 10^13 gc/mL
recombinant DNA reagent	AAV5-hSyn-DIO-hM3D(Gq)-mCherr	Addgene	44361	2.6 x 10^13 gc/mL
sequence-based reagent	*Oxt*	ACD Bio	454011	(1:2)
sequence-based reagent	*Fos*	ACD Bio	316921	(1:2)
software, algorithm				
other	cholera toxin subunit B conjugated with Alexa Fluor 647	Invitrogen	C34778	0.50%